Insights into sulfur cycling at subduction zones from *in-situ* isotopic analysis of sulfides in high-pressure serpentinites and 'hybrid' samples from Alpine Corsica

R.J. Crossley[1, 2*], K.A. Evans[1], H. Jeon[3, 4] & M.R. Kilburn[3]

[1]School of Earth and Planetary Sciences, Curtin University, GPO Box U1987, Perth, WA 6845, Australia.

[2]Present address: School of Geosciences, University of the Witwatersrand, Private Bag 3, 2050 Wits, Johannesburg, South Africa.

[3]Centre for Microscopy, Characterisation and Analysis, University of Western Australia, Crawley, WA 6009, Australia.

[4]Present address: Department of Geosciences, Swedish Museum of Natural History, Box 50 007, SE-10405 Stockholm, Sweden.

*corresponding author: Rosalind.Crossley@wits.ac.za

Keywords

Sulfur; Subduction; Stable isotope; In-situ; Serpentinite; Redox

1

Abstract

Devolatilisation of serpentinites at depth in subduction zones contributes significant quantities of sulfur and other redox sensitive elements to the sub-arc mantle. However, the fate of sulfur in subducted serpentinites is poorly constrained. Textures of sulfur-bearing phases in subducted serpentinites are rarely studied, yet provide important information on the changes to sulfur distribution throughout the subduction cycle and as a result of fluid infiltration. $\delta^{34}S$ values of sulfides provide constraints on sulfur sources, the redox state of sulfur in the host mineral, and on processes that have occurred subsequent to sulfide crystallisation, including interaction with oxidised or reduced fluids. Therefore, it is possible to use $\delta^{34}S$ values in subducted serpentinites to constrain the redox state of sulfur in sulfides and subduction zone fluids. Furthermore, the proximity of serpentinites to ocean crust and metasediments may influence enrichment or depletion of ^{34}S during subduction relative to serpentinites distal to such lithologies.

This study investigates the redox state, the likelihood of sulfur addition to the sub-arc mantle from serpentinite dehydration, and the distribution of sulfur within subducted serpentinites and 'hybrid' mafic/ultramafic rocks from Alpine Corsica. The techniques utilised include petrographic analysis, *in-situ* sulfur isotopic analysis and trace element analysis of sulfides hosted in these rocks. All sulfides investigated have high $\delta^{34}S$ values of 1.9–15.5‰, which suggests that mantle-derived sulfur ($\delta^{34}S \sim 0.1$‰), was not the sole source of sulfur. The highest $\delta^{34}S$ values are recorded in pyrites of a hybrid mafic/ultramafic sample. High $\delta^{34}S$ values are preserved in sulfides attributed to prograde metamorphism, and is most consistent with the retention of sulfur derived from hydrothermal sulfate reduction on the seafloor. However, a shift towards higher $\delta^{34}S$ values in sulfides associated with the advanced stages of exhumation suggests that late stage exhumation enables enhanced access to slab-derived fluids bearing oxidised sulfur (SO_4^{2-} or SO_2). Such fluids may have been derived from the devolatilisation of serpentinite at greater depth, or from other lithologies.

1. Introduction

Sulfur is subducted in variable oxidation states from sulfate (+6) to sulfide (-2) within altered ocean crust, hydrated mantle lithosphere and ocean floor sediments, to contribute a significant flux of redox budget to subduction zones (Evans, 2006; Evans, 2012). Sulfur input

2

5   to subduction zones is an order of magnitude higher than the flux of sulfur released (Evans,

6   2012; Evans et al., 2014). However, changes to the oxidation state of sulfur, the processes

7   that sulfur undergoes during subduction and the quantity of sulfur transferred to the sub-arc

8   mantle and deep mantle are poorly constrained (e.g., Evans et al., 2014). The redox state and

9   the concentration of sulfur in the sub-arc mantle are of particular importance because genetic

10   models for arc-related ore deposits currently require an oxidised sub-arc mantle (e.g.,

11   Mungall et al., 2002).

12   The combined approach of sulfide mineral paragenesis and *in-situ* measurement of

13   sulfur isotopes (δ^{34}S) in sulfur-bearing mineral phases within rocks that have undergone

14   subduction and, at a later stage, exhumation, can be used to constrain the source, redox state

15   and processes that sulfur has undergone throughout the subduction cycle. Such processes

16   include bacterial sulfate reduction, fluid infiltration or devolatilisation. ^{34}S partitions

17   preferentially into oxidised species relative to ^{32}S; for example, present day seawater sulfate

18   has a δ^{34}S value of ~20–21‰ (Rees, 1978; Paytan et al., 1998, 2004; Tostevin et al. 2014),

19   whereas mantle sulfur is 0.1±0.5‰ (Sakai et al., 1984; Shanks et al., 1995; Alt and Shanks,

20   1998). The observation that porphyry arc-related ore deposits have δ^{34}S values up to ~13‰

21   higher than the mantle (Alt et al., 1993; Ishihara & Sasaki, 1989), requires a source of ^{34}S,

22   which is proposed to have originated via sulfate transfer from the slab (Richards, 2015). Pre-

23   subduction fixation of sulfate in serpentinised mantle lithosphere, oceanic crust and

24   sediments is considered to account for sulfate enrichment in the slab (Ishihara and Sasaki,

25   1989; Shanks et al., 1981; Wallace & Edmonds, 2011; Alt et al., 2012a; Debret et al., 2014;

26   Evans et al., 2014). However, sulfur release and retention within the slab during subduction,

27   and the mechanisms that control the distribution of sulfur are not well understood.

28   Attempts have been made to constrain subduction-related fluxes of sulfur from the

29   oceanic crust (Evans et al., 2014; Marschall & Shimizu, 2012; Aulbach et al., 2012), but

30   fluxes from the hydrated mantle lithosphere during subduction are rarely investigated, with

31   some exceptions (e.g., Alt et al., 2012a; Alt et al., 2012b; Shimizu et al., 2013). The hydrated

32   mantle lithosphere component of the slab is of particular interest because its dehydration at

33   depth within the subduction channel has the potential to release a significant volume of

34   fluids, which could migrate to the sub-arc mantle. Various processes can affect the sulfur

35   isotope composition of peridotite exhumed on the seafloor at spreading centres, including

36   microbial sulfate reduction (Alt and Shanks, 1998; Alt et al., 2007; Schwarzenbach et al.,

37   2012; Ono et al., 2012) and hydrothermal sulfate reduction (Alt and Shanks, 2003; Bach et

al., 2004, Alt et al., 2007, Delacour et al., 2008; Peters et al., 2010, Ono et al., 2012). Temperature governs the process that prevails on the seafloor (e.g., Schwarzenbach et al., 2018). A contribution from seawater-derived sulfate in modern day can result in ^{34}S-enriched serpentinites with δ^{34}S values of up to ~20‰ compared to the Earth's mantle (Delacour et al., 2008; Alt & Shanks, 2003; Alt et al., 2012a, Tostevin et al., 2014). Therefore, upon subduction, serpentinites may carry oxidised sulfur to the sub-arc mantle or deep mantle. In contrast, microbial sulfate reduction on the seafloor at low temperature results in a ^{34}S depleted reservoir of reduced sulfur, and resultant δ^{34}S values as low as -34‰ (Alt and Shanks, 1998; Schwarzenbach et al. 2012). Therefore, the oxidation state of sulfur input into subduction zones is strongly dependent on temperature, whether the system is open or closed with respect to sulfur, and whether microbial or hydrothermal processes govern sulfate reduction.

Δ^{33}S is used to describe the extent of mass independent fractionation (MIF); the degree to which variations in isotope abundance are not dependent on mass. Δ^{33}S values provide additional information compared to the measurement of δ^{34}S values alone (Ono et al., 2012; Schwarzenbach et al., 2018), and allows distinction between open and closed system sulfate reduction, and between bacterial sulfate reduction and hydrothermal sulfate reduction that can be traced through subduction. Non-zero MIF values for sulfur indicate that the analysed sulfur deviates from the terrestrial line defined by the slope of a fractionation line between δ^{34}S and δ^{33}S for the Earth-Moon system, where the slope is 0.515 (Seal, 2006 and references therein). Modern day seawater sulfate has a Δ^{33}S value of 0.050±0.0003‰ (Ono et al., 2012), whereas mid ocean ridge basalts (MORB) from the East Pacific Rise have Δ^{33}S values within error of zero at ~0.001±0.017‰ (Ono et al., 2012). A study of samples from the Iberian Margin basement revealed that serpentinised peridotites have higher Δ^{33}S values than basaltic samples with values ranging from 0.00 to 0.16 in peridotites (Ono et al., 2012; Schwarzenbach et al., 2018), compared to -0.06 to 0.04 in the basalts (Ono et al., 2012). Lower Δ^{33}S values (-0.06 to 0.02) have been reported for Northern Appenine serpentinites (Schwarzenbach et al., 2018), and similarly low Δ^{33}S values (-0.01 to 0.01) are reported for basalts from the Pacific-Antarctic ridge, however, these values are indistinguishable from the Canyon Diablo Troilite international standard (Labidi et al., 2014).

The proximity of serpentinites to ocean crust and metasediments in the subduction channel may influence the redox state and concentration of sulfur in both serpentinites and other lithologies, and therefore the sulfur isotope compositions, either through the loss of

4

71 oxidised or reduced fluids from serpentinites, or the infiltration of fluids from other

72 lithologies. For example, seafloor serpentinites associated with gabbroic intrusions have been

73 shown to have higher δ^{34}S values than serpentinites elsewhere (Alt and Shanks, 2003).

74 Mixing of sediments/oceanic crust and mantle along the slab/sub-arc mantle interface at high-

75 pressure produces 'hybrid' rocks, which are physical or chemical mixtures of two or more

76 end member rock types, such as sediment, peridotite (mantle), gabbro and basalt (Spandler

77 and Pirard, 2013; Marschall and Schumacher, 2012), and have chemical and isotopic

78 compositions that reflect this mixing. Hybrid rocks have been recognised as important

79 carriers of volatile elements to even greater depths than the serpentinised mantle (e.g.,

80 Spandler et al. 2008), and could play an essential role in the transfer of sulfur to the sub-arc

81 mantle.

82 Although whole rock δ^{34}S data are available for subducted ultramafic rocks (Alt et al.,

83 2012a; b), subducted ultramafic rocks undergo several stages of alteration starting at the

84 seafloor, followed by subduction and exhumation, such that whole rock sulfur isotope

85 analysis provides a record of superimposed processes. *In-situ* δ^{34}S measurements of sulfides

86 with well-constrained parageneses provide an opportunity to sample the evolution of sulfur

87 throughout the metamorphic evolution of the samples. To the authors' best knowledge the

88 only other published *in-situ* δ^{34}S values for subducted ultramafic rocks are reported in two

89 conference abstracts, Santiago-Ramos et al. (2012) and Shimizu et al. (2013) who measured

90 δ^{34}S values of pentlandite and heazlewoodite grains within Erro Tobbio serpentinites. These

91 studies report relatively low δ^{34}S values for sulfide grains within low temperature

92 serpentinites (-3.2 to 5.9‰), and variable δ^{34}S values from -1.1 to 18.3‰ for sulfide grains

93 within subducted serpentinites.

94 In this study, redox conditions, the likelihood of sulfur transfer to the sub-arc mantle

95 from serpentinite dehydration, and the distribution of sulfur within subducted serpentinites

96 and hybrid mafic/ultramafic rocks are investigated through a combination of petrographic

97 analysis, *in-situ* sulfur isotope and trace element analyses of sulfides hosted in these rocks.

2. Geological Background

99 Thirty samples were collected from the Schistes Lustrés complex at the two localities

100 Serra di Pigno and Capu Corvoli, Cap Corse (Fig. 1). Serra di Pigno lies approximately 10

101 km west of Bastia, on Cap Corse (Fig. 1a). The sample collection includes metagabbros,

102 metasediments, serpentinites and hybrid rocks from the Schistes Lustrés complex.

5

103 Serpentinite samples from Serra di Pigno were collected adjacent to metasediments, 104 metagabbros and metabasalts, and distal to these lithologies (Fig. 1b, c). Hybrid samples from 105 Capu Corvoli were collected from slivers next to metagabbro and <0.5 km from calcareous 106 schist (Fig. 1d, e). These localities were chosen because they allow the assessment of 107 lithological controls on the isotopic composition of sulfur.

108 During the Middle to Late Jurassic, the ophiolites and associated sediments were 109 considered to have been part of an ocean-continent transition (OCT) zone (e.g., Vitale 110 Brovarone and Herwartz, 2013; Vitale Brovarone et al., 2013; Magott et al., 2016). At this 111 time, seawater sulfate had $\delta^{34}S$ values of ~ 17‰ (Kampschulte and Strauss, 2004). Field 112 observations consistent with an OCT setting of the ophiolites prior to subduction include the 113 juxtaposition of continental slices and ultramafic rocks, ultramafic clasts within carbonaceous 114 sediments, the presence of ophicalcites, and variable interlayering of sediments with mafic 115 and ultramafic lithologies at Serra di Pigno (Meresse et al., 2012) and other localities within 116 Alpine Corsica (Vitale Brovarone et al., 2011).

117 The samples from the Serra di Pigno region record blueschist to eclogite facies 118 metamorphism and underwent high-pressure metamorphism from ~55 to 34 Ma (Ravna et al., 119 2010; Vitale Brovarone et al. 2011, Vitale Brovarone and Herwartz, 2013). The minimum 120 pressure recorded during subduction is estimated to be ~1.3–2.6 GPa (Lahondère and 121 Guerrot, 1997; Vitale Brovarone et al., 2013), and on the basis of Raman spectroscopy of 122 carbonaceous material (Vitale Brovarone et al., 2013), the peak metamorphic temperature is 123 constrained to ~414–471℃.

124 The chlorite schist and talc schist hybrid mafic/ultramafic samples were collected at 125 Capu Corvoli, Cap Corse. The samples are from a shear zone with a top-to-the-west to 126 northwest sense of shear, parallel to a series of proximal WNW to NW shallowly dipping 127 thrust faults, which were previously interpreted to divide the lawsonite-blueschist Upper 128 Castagniccia metasediments and lawsonite-eclogite ophiolites (Lahondère, 1992). The sense 129 of shear is uniform with deformation associated with prograde metamorphism (Mattauer et 130 al., 1977; 1981; Faure and Malavielle, 1981; Harris, 1985; Warburton, 1986; Magott et al., 131 2016). Within the shear zone, slivers of the hybrid lithologies are juxtaposed with 132 metagabbro. Recent P-T estimates suggest that the Upper Castagniccia metasediments record 133 eclogite facies metamorphism (Vitale Brovarone et al., 2013 & references therein). Thus, the 134 Capu Corvoli samples record similar or higher P-T conditions than the Serra di Pigno

6

135 samples at ~490–550 °C and 1.9–2.6 GPa (Ravna et al., 2010; Vitale Brovarone et al., 2011;
136 2013).

137   In this study, existing estimates of P-T conditions (e.g., Agard and Vitale-Brovarone,
138 2013), detailed sample petrography and mineral chemistry are used to distinguish between
139 sulfides associated with mantle, seafloor, prograde, peak and retrograde stages. In the
140 seafloor environment, sulfur is present as mantle sulfides, or as sulfides derived from
141 seawater sulfate and precipitated during hydrothermal alteration. Such sulfides could be
142 preserved during prograde metamorphism, or these sulfides may recrystallize at this stage.
143 The onset of exhumation is marked by a decrease in pressure (Agard and Vitale-Brovarone,
144 2013). At this stage, maximum temperatures are recorded, such that heating via continued
145 thermal equilibration is still occurring at the onset of exhumation. Additionally, it is likely
146 that the rocks remain partially hydrated even after they have undergone prograde
147 metamorphism, therefore, therefore fluids are also released at the onset of exhumation (e.g.,
148 Miller and Cartwright, 2006). Hence, the rocks may have access to both prograde and
149 exhumation-related fluids during this stage. Retrogressed sulfides associated with such fluids
150 provide insight into the composition of fluids released from the slab.

3. Petrography

152   Different sulfide generations are attributed to stages of metamorphism on the basis of
153 their textural association with silicate minerals, where silicate mineral stability has been well
154 constrained at a range of temperatures and pressures. Primary sulfides are typically
155 polyhedral blebs with concave inward boundaries (Seyler et al., 2007; Schwarzenbach et al.,
156 2012), a textural characteristic that is not observed in any of the samples. In this section, the
157 numbering 1-3 is used to assign sulfides to stability during (1) prograde metamorphism (2)
158 the onset of exhumation, and (3) advanced stages of exhumation.

3.1 Serra di Pigno

3.1.1 Serpentinite CO13-40

161   CO13-40 is a serpentinite sample distal to other lithologies (grid reference: WGS 84,
162 zone 32T, 0533122 mE 4728302 mN, Fig. 1 a, b). Pentlandite1 (pn1) consist of grains up to
163 ~50 μm in diameter associated with magnetite. Both magnetite and pn1 overprint the foliation
164 defined by fine-grained antigorite (atg1), and contain inclusions of atg1 (Fig. 2a). Orientated
165 and foliated antigorite (atg1) has a fine and interlocking texture consistent with prograde

166 growth (e.g., Li et al., 2004), and defines the dominant foliation. Given the inclusion of atg1

167 in pn1, it is inferred that pn1 maintained stability during prograde to peak metamorphism. A

168 late generation of antigorite (atg2) cuts pn1 (Fig. 2a) and therefore further constrains pn1

169 growth to a stage prior to retrogression.

3.1.2 Serpentinite CO13-33

171 CO13-33 is a serpentinite sample collected from an outcrop proximal to metagabbro

172 and metaquartzite (grid reference: WGS 84, zone 32T 0533514 mE 4729532 mN, Fig. 1a, b).

173 Early pentlandite (pn1; Fig. 2b) occurs as elongate grains (~5 μm) associated with

174 heazlewoodite, magnetite1, kamacite (~5 μm), fine matrix antigorite and fine balangeroite

175 veins (<5 μm across). Balangeroite growth has previously been ascribed to prograde

176 metamorphism within the antigorite stability field in both the Piemonte zone in the Alps

177 (Groppo and Compagnoni, 2007), and Sasaguri, Japan (Evans and Kuehner, 2011). The

178 association of pn1 with fine-grained antigorite (atg1) and balangeroite implies that pn1 was

179 stable during prograde metamorphism. Chlorite growth is associated with antigorite

180 dehydration (e.g., Padrón-Navarta et al., 2013; Scambelluri et al., 2014; Evans and Powell,

181 2015), overprinting atg1. Pentlandite2 partially replaces chlorite (pn2; Fig 2c) and contains

182 inclusions of atg1. Therefore, pn2 postdates prograde–peak metamorphism and is considered

183 to have grown at the onset of exhumation, overprinted by a later generation of magnetite at

184 the rim. A late phase of pentlandite, pn3, occurs as euhedral to subhedral grains that overprint

185 a late generation of antigorite veins, and is synchronous with or includes late magnetite (Fig.

186 2d), thus pn3 is related to advanced stages of exhumation.

3.1.3 Serpentinite CO13-55

188 CO13-55 is a serpentinite sample proximal to metagabbro and calcareous schist (grid

189 reference: WGS 84, zone 32T, 0533398 mE 4729368 mN, Fig. 1a, b). Primary phases are

190 absent; all spinel grains are 'porous', Al-poor, Cr-Fe spinel with mt1 rims, which are

191 compositionally and texturally consistent with alteration of primary spinel during seafloor

192 and/or prograde metamorphism (Evans and Frost, 1975; Bliss and MacLean, 1975; Wylie et

193 al., 1987; Kimball, 1990; Frost, 1991; Barnes, 2000; Mellini et al., 2005; Merlini et al., 2009;

194 Mukherjee et al., 2010; Grieco and Merlini, 2012; Gervilla et al., 2012; Colás et al., 2014).

195 Phases stable during prograde to peak metamorphism include fine-grained antigorite (atg1),

196 which comprises the matrix (<1 to 5 μm), chlorite, pentlandite1 (pn1), pyrite and

197 chalcopyrite. Altered porous spinels contain inclusions of fine-grained antigorite (atg1) and

8

198 pentlandite (pn1), consistent with the interpretation of recrystallisation of antigorite from
199 precursor lizardite and retention of pn1 during prograde metamorphism. Pentlandite1 also
200 consists of larger grains (10–30 μm), which contain small Cr-Fe spinel grains (2–3 μm) and
201 overprints or is in equilibrium with mt1 but is itself cut by atg2 veins (Fig. 2e). Phases
202 associated with the onset of exhumation include pentlandite2 (pn2) and mt2. Pentlandite2 and
203 mt2 are associated with diopside, although some grains of diopside are observed overprinting
204 these phases. Diopside growth is constrained to the onset of exhumation, or after, because it
205 overprints prograde antigorite and peak chlorite. Additionally, diopside is comprised of
206 randomly orientated idioblastic prims (Fig. 2f, g) consistent with retrograde textures
207 previously described elsewhere (Groppo and Compagnoni, 2007). Pentlandite3 is
208 synchronous with or occurs as rims on late antigorite cross-cutting veins (Fig. 2h) and
209 therefore pn3 postdates the veins (Fig. 2h), where antigorite veins cut prograde to peak
210 phases (pyrite, chalcopyrite, pn1 and mt1) (Fig. 2e), and phases associated with the onset of
211 exhumation (pn2 and mt2).

212 **3.2 Capu Corvoli**

213 *3.2.1 Chlorite schist CO14-03*

214 CO14-03 is a chlorite schist in contact with metagabbro that lies structurally above the
215 sample (grid reference: WGS 84, zone 32T, 0529140 mE 4753069 mN; Fig. 1d, e). There is
216 little evidence for the retention of primary or seafloor phases. The earliest phases associated
217 with prograde to peak metamorphism are thin (<5 μm), orientated laths of foliated chlorite
218 and antigorite, which together comprise the matrix. Magnetite is constrained to the onset of
219 exhumation because it cuts the prograde to peak antigorite-chlorite defined foliation.
220 Magnetite has undergone brittle deformation and is cut by second generation of chlorite
221 (chl2) veins, and overprinted by titanite, a low-pressure Ti-rich phase (e.g., Laird & Albee,
222 1981; Spear, 1981; Ernst & Liu, 1998). Thus, magnetite growth is constrained to the earliest
223 stages of exhumation. Pyrite occurs as euhedral aggregates isolated in the matrix, as rims on
224 magnetite or within fractures connected to the matrix in magnetite (Fig. 2i, j). Pyrite is
225 enclosed by titanite, although some grains contain inclusions of titanite towards the rim
226 implying synchronous pyrite and titanite growth for some time. Pyrite is therefore attributed
227 to lower pressures associated with an advanced stage of exhumation, and is thus referred to as
228 py3.

3.2.2 *Talc schist CO14-04*

229

230   CO14-04 is a talc schist sample in contact with metagabbro associated with CO14-03

231   structurally below the sample (grid reference: WGS 84, zone 32T, 0529107 mE 4753071 mN,

232   Fig. 1d, e). Primary or seafloor phases consist of an early generation of pyrrhotite (po0 <5

233   μm), Cr-rich spinel cores to magnetite, and Pt-rich alloys (rare, ~2 μm). Cr-Al spinels are

234   proposed to be primary based on their Al-rich composition (e.g. Barnes and Roeder, 2001),

235   although the grains could have undergone alteration during seafloor alteration from more Mg-

236   rich primary compositions. The association of spinel with pyrrhotite0 and Pt-rich alloys

237   attributes these phases to primary growth and possible alteration during seafloor processes.

238   Prograde phases include pyrite (py1), an early generation of talc (talc1), magnetite, a later

239   generation of pyrrhotite (po1) and chlorite. Talc1 growth is attributed to metasomatism

240   during subduction (e.g., Spandler et al., 2008). Pyrite1 contains inclusions of pyrrhotite0, Cr-

241   Al spinel and a Pt-rich alloy. Given the inclusion of Cr-spinel in py1, and magnetite rims on

242   Cr-rich spinel, py1 and magnetite growth are synchronous. Chlorite, which is attributed to

243   peak metamorphism, cross-cuts magnetite, thus the growth of magnetite and py1 predate peak

244   metamorphism. Pyrrhotite1 is texturally later than py1, given its inclusion in rims on py1,

245   though possible incorporation from the matrix cannot be excluded. A second generation of

246   pyrite (py2) cuts the prograde talc1 matrix and peak metamorphic chlorite, and has coarse

247   talc2 rims (Fig. 2i). Talc stability is restricted to pressures below 1.5 GPa (Evans & Powell,

248   2015), therefore the talc rim records decompression associated with advanced stages of

249   exhumation (e.g., Crossley et al., 2017). Pyrite2 is therefore constrained to growth during the

250   onset of exhumation.

4. Methods

251

252   The samples selected for this study contain sulfides of suitable size for secondary ion

253   mass spectrometry (SIMS) analysis, using a large geometry (LG) SIMS, a Cameca IMS 1280,

254   and NanoSIMS. Prior to *in-situ* analysis, detailed petrographic analysis was undertaken using

255   transmitted and reflected light microscopy, and scanning electron microscopy (SEM) and

256   energy dispersive spectrometry (EDS). Electron probe microanalysis (EPMA) was performed

257   prior to SIMS analysis to determine compositions of sulfides. In addition, EPMA and

258   NanoSIMS mapping were employed to search for any discrete zoning in sulfide minerals.

4.1 Sample Preparation

Prior to SIMS and NanoSIMS analysis, representative areas were selected from thin section billets, where billets were cut perpendicular to sample foliation, and drilled from each sample using a hollow cylindrical diamond coated drill bit that produces 7 mm pucks. The pucks were mounted in 25 mm diameter epoxy disks, polished and coated with ~30 nm of Au to provide electrical conductivity at high voltage and thus prevent sample charging. Using a precision saw, the mounts were trimmed by approximately one third to allow a reusable standard piece that contains Sierra pyrite and VMSO pentlandite standards to be mounted alongside the unknown samples in the ion probe.

4.2 EPMA Mapping

Trace element mapping was carried out on sulfide grains selected for SIMS analysis using the JEOL 8530F Hyperprobe at the Centre for Microscopy, Characterisation and Analysis (CMCA) at the University of Western Australia (UWA). The carbon coating was 25 nm in thickness. Wavelength dispersive spectrometry (WDS) operating conditions included a 20 kV accelerating voltage, a 20 nA beam current, and a 40s dwell time. Mean atomic number (MAN) background corrections were used with a total on-peak counting time of 20 s per element. The standards used for calibration include Ni, Co, Pyrite (S) and ASP200 (arsenopyrite; As). WDS was conducted using the crystals PETJ for S Kα, TAP for As Lα, and LiF for Fe Kα. The use of two crystals, LiFH and LiF, enabled optimum detection of Co Kα and Ni Kα. Data reduction was performed using the Probe for EPMA software (Donovan et al., 2012), and quantitative element maps were generated from WDS X-ray intensity maps using the CalcImage and Surfer 10.2 software. A matrix correction was conducted at each pixel and a script file was output for each element. Element concentrations were calculated using the mean atomic number (MAN) background method, where after background correction, X-ray intensity was multiplied by the matrix effect correction factors Z (atomic number correction; Duncumb and Reed, 1968), A (absorption correction; Philibert, 1963; Duncumb & Shields; 1966; Heinrich, 1969; Bearden, 1964; Heinrich, 1986) and F (characteristic fluorescence correction; Reed, 1965), relative to standards. The script files generated by CalcImage were input into Surfer 10.2 to plot maps for each element.

Point analyses were carried out under the same operating conditions but additional standards were used for calibration including wollastonite (Si), San Carlos Olivine (Mg), Crocoite (Pb), ZnO, Cu, Mn, Cr_2O_3, Bi_2Se_3, Ag, GaAs (As), and Sb. In addition, WDS was

11

conducted using the crystals LiF for Ni Kα and Co Kα, TAP for Si Kα, Mg Kα and Se Lα, PETJ (Pb mα), LiFH (Zn Kα, Cu Kα, Mn Kα, Cr Kα), PETJ (Ag Lα and Bi Mα) and LiF (Sb Lα).

4.3 Secondary Ion Mass Spectrometry

4.3.1 NanoSIMS

Mapping of small pentlandite grains in sample CO13-40 was performed on the CAMECA NanoSIMS N50 at the CMCA, UWA, prior to LG-SIMS analysis. Secondary ion images were acquired using a focused Cs^+ primary ion beam, with a nominal beam diameter of ~100 nm. Electron multipliers at the five detector sites were positioned to detect the secondary ions FeS^-, CoS^-, NiS^-, CuS^-, AsS^-, Te^- and Au^- on masses 88, 91, 92, 97, 107, 130 and 197, respectively. The mass spectrometer was tuned using a 30 μm entrance slit, and peak positions were calibrated using sulfide minerals and metallic Au. Areas of 60×60 μm and 30×30 μm were imaged at a pixel resolution of 512×512, with a primary beam current of approximately 2.8 pA, and a dwell time of 25 ms/pixel. Smaller areas of 15×15 μm were imaged at a pixel resolution of 256×256, with a primary beam current of approximately 1.2 pA and a dwell time of 45 ms/pixel. All areas were pre-sputtered to 10^{17} Cs ions/cm^2 prior to imaging. All images were corrected for 44 ns detector deadtime and processed using the NRIMS plugin for ImageJ (http://nrims.harvard.edu/software).

4.3.2 LG-SIMS: Cameca IMS 1280

4.3.2.1 Standards

Sierra pyrite (fragments from the same pyrite block have been previously reported as Sonora-3) is from a 9 kg cube of pyrite from a Cretaceous porphyry copper mine in Sonora, Mexico, described in Wacey et al. (2011), Farquhar et al. (2013) and Evans et al. (2014). VMSO pentlandite is sourced from a massive sulfide lens from the Ni-Cu-PGE Long-Victor mine, Kambalda, Western Australia metamorphosed to amphibolite facies (Barnes et al., 2013, and references therein). All $\delta^{34}S$ values in this study are relative to Vienna Canyon Diablo Troilite (VCDT), the value of which is assumed to be 0.0450045 (Ault and Jensen, 1963). The details of bulk $\delta^{34}S$ measurement by laser fluorination, heterogeneity, precision and reproducibility of the Sierra pyrite and VMSO pentlandite standards are discussed in detail in LaFlamme et al. (2016). Both Sierra and VMSO are of similar major element (Fe, Ni, Co and S) compositions to the pyrites and pentlandites studied here (section 5.1).

12

4.3.2.2 Method

323   Ion microprobe analysis was carried out on the CAMECA IMS 1280 at the CMCA,

324   UWA, to measure *in-situ* sulfur isotope compositions ($^{33}S/^{32}S$ and $^{34}S/^{32}S$). A ca. 2–3 nA

325   focused Cs^+ primary beam was operated at 10 kV and the secondary ion beam was extracted

326   at -10 kV. The analysis area was presputtered using a 25×25 μm (or 20×20 μm for

327   pentlandite) raster for 30 seconds (or 10 sec for pentlandite; see below) followed by

328   automated secondary centering in the field aperture (FA; 4000 μm) and entrance slit (ES; 60

329   μm). The analysis used a 15×15 μm (or 10×10 μm for pentlandite) raster employing

330   dynamic transfer at a $133 \times$ field magnification for 45×4 second integrations. Three sulfur

331   isotopes were measured simultaneously using three Faraday Cup detectors with amplifiers of

332   10^{10} Ω resistor for ^{32}S and 10^{11} Ω for ^{33}S and ^{34}S. An exit slit of 500 μm was used on each of

333   the multicollector detectors, providing a nominal mass resolving power (MRP) of ca. 2500.

334   As this MRP does not allow for complete resolution of the ^{32}S ^1H and ^{33}S peaks, the detector

335   collecting ^{33}S was offset to the low mass side, sufficient to exclude tailing of the ^{32}S ^1H signal

336   (e.g., LaFlamme et al., 2016). The magnetic field was regulated using nuclear magnetic

337   resonance (NMR). To avoid any problems related to non-conducting inclusions and/or to the

338   very small pentlandite grains in the silicate matrix, a normal incidence electron gun was used

339   for charge compensation in all analyses. Although ^{36}S was not analysed, an electron

340   multiplier detector was also setup to locate pentlandite grains <20 μm using the ^{36}S ion

341   image. For these pentlandite analyses, the areas were pre-burnt to see their ion images so the

342   presputter time was reduced to 10 seconds. Measurements of an appropriate standard after

343   each block of four to five analyses allowed the assessment of instrumental drift. The method

344   for data reduction is described in Appendix A.

345   Incorporation of minute antigorite inclusions in the analysis volume (<2 μm) may

346   have affected S isotope ratios via the changes to matrix fractionation effects, however the

347   inclusions would not contain sufficient sulfur to alter $\delta^{34}S$ values. Sulfide grains were

348   checked carefully for such inclusions using SEM and nominally inclusion-free areas were

349   analysed. After the measurements were finished, the analysed spots were checked again using

350   SEM.

5. Results

5.1 Sulfide mineral compositions

Average major element concentrations for sulfides are provided in Table 1. The full dataset is provided in Appendix B. Formulae of sulfide minerals were calculated using charge balance and stoichiometric constraints. Different generations of sulfides are indistinguishable on the basis of mineral composition. The average mineral formulae for pentlandite in CO13-33 and CO13-55 is $Fe_{3.5–3.9}Ni_{4.8–5.2}Co_{0.3}S_8$ ($n = 36$ and 30, respectively). Pentlandite in CO13-40 has higher concentrations of Fe and contains lower concentrations of Ni and slightly lower Co concentrations with the average formula $Fe_{4–4.2}Ni_{4.6–4.8}Co_{0.2–0.3}S_8$. Pyrites in CO14-03 and CO14-04 are stoichiometric (FeS_2) with minor (up to 0.01 cations) Co and Ni replacing Fe per formula unit in each sample.

5.2 Sulfur isotope compositions and trace element mapping

Here the results are presented as $\delta^{34}S$ values, non-zero $\Delta^{33}S$ values, and EPMA trace element maps. The complete sulfur isotope data set including the $\delta^{33}S$ values and measured standard sulfur isotope compositions are provided in Appendix C. All uncertainties reported in the text, figures and tables are 2σ, unless otherwise noted.

5.2.1   Serra di Pigno

5.2.1.1 Distal Serpentinite CO13-40

$\delta^{34}S$ values in CO13-40 pentlandite range from 4.3 to 10.4‰ (n=30) (Fig. 3a, Fig. 4a–e, Table 2, Appendix C). Three analyses have non-zero $\Delta^{33}S$ values of 0.52±0.30‰ (a3_s12-3), 0.67±0.50‰ (a3_s1-2) and 0.38±0.24 ‰ (a3_s3) (Table 3). Trace element NanoSIMS maps reveal zonation in Cu, Co, As and Ni. Co, As and Ni zoning is decoupled from the Cu zoning (Fig. 4f). Due to the small size of the grains (up to 50 μm), it was not possible to determine the relationship of the zonation to the $\delta^{34}S$ ratios, therefore homogeneous areas were chosen for analysis.

5.2.1.2 Serpentinite proximal to metaquartzite and metagabbro CO13-33

$\delta^{34}S$ values in pentlandite in CO13-33 range from 1.8 to 9.2 ‰ (n = 18) (Table 2, Appendix C; Fig. 3b; Fig. 5a–e). The sulfides analysed include pn1 (n=9; Fig. 5a, b), pn2 (n=9; Fig. 5b, c) and pn3 (n=5; Fig. 5d–e). The histograms display a unimodal distribution (Fig 3b) and Mann-Whitney U tests (Appendix D) do not reveal significant variation in $\delta^{34}S$ between the different generations of pentlandite from early to late grains. Pn1 grains have

14

382 similar δ^{34}S values to pn2 grains with values of 6.5 to 8.8‰ in pn1 grains, compared to 5.5 to

383 8.3‰ in pn2 grains ($p = 0.79$), where p indicates the probability that the pn1 and pn2

384 analyses are from the same distribution. δ^{34}S values of pn3 grains vary from 1.8–8.4‰, and

385 are not significantly different from pn1 and pn2 ($p = 0.39$). EPMA mapping reveals

386 homogenous Co concentrations in the interior of pn2, but higher Co concentrations towards

387 pn2 rims, (Fig. 5f).

5.2.1.3 Serpentinite proximal to calcareous-schist and metagabbro (CO13-55)

389   δ^{34}S values in pentlandite within CO13-55 range from 1.9 to 8.0‰ (n=19; Table 2,

390 Appendix C, Fig. 3c); pn1 from 1.9 to 5.7‰ (n=10; Fig. 6a–c), pn2 δ^{34}S from 3.1–6.9‰

391 (n=5; Fig. 6d) and pn3 from 5.5–8.0‰ (n=5; Fig. 6e–f). The Mann Whitney U test revealed a

392 significant difference between pn1 and pn3 at a level of significance of 1% ($p = 0.0078$), but

393 not between pn2 and pn3 ($p = 0.05$). Four analyses have non-zero Δ^{33}S values of 0.33±0.23‰

394 (area2_s1-1, pn1), 0.37±0.28‰ (area2_s3-1; pn2), 0.38±0.23‰ (area3_s2-1, pn3) and

395 0.49±0.31‰ (Table 3, pn1). Zonation in Co is not evident in CO13-55 pentlandites (Fig. 6b).

5.2.2   Capu Corvoli

5.2.2.1 Chlorite Schist CO14-03

398   Relative to other samples in this study, CO14-03 pyrite δ^{34}S values are very

399 heterogeneous, within individual pyrite grains and between different pyrite grains, with

400 values ranging from 5.9 to 15.5 ‰ (n=32; Table 2, Appendix C, Fig. 3d). The majority of

401 grains have δ^{34}S values from 6–9‰ (n = 21), with higher δ^{34}S values from 10.8–15.5 ‰ (n =

402 11). Some pyrites appear to form clusters, while others are isolated in the matrix. Although

403 no differences in relative timing are inferred from textural analysis, isolated pyrites (Fig. 7 a–

404 c, n=17) were compared to pyrites in clusters (Fig. 7d–e, n=15). Significantly higher δ^{34}S

405 values were recorded in pyrite that formed clusters ($p = 0.0057$). EMPA mapping reveals fine

406 scaled zonation of Co from 0.1 to 1.2 wt%, and of Ni from 0.1 to 0.4 wt% (Fig. 8a–c). The

407 Co and Ni zonation does not show a significant correlation with δ^{34}S ($R^2 = 0.3$ and 0.23,

408 respectively, Fig. 8d).

5.2.2.2 Talc Schist CO14-04

410   CO14-04 pyrites appear to be relatively homogeneous with δ^{34}S values of 3.6–5.4‰

411 (n=49). Py1 has slightly higher values (4.1–5.4‰, n=12; Fig. 9a–d), compared to py2 which

412 has a larger range from 3.1–5.0‰ (n=37; Fig. 9e–f), where there is a low probability of both

413 pyrite generations sampling the same isotopic population (p=0.0065). Additionally, three

15

414 $\Delta^{33}S$ values are significantly different to zero, s1 in area 1 (0.11±0.10‰), s1 analysis 9 in
415 area 2 (-0.16±0.12‰) and S1 in area 3 (-0.17±0.15‰).

416   EPMA maps show Co and Ni zonation at a finer scale than the interaction volume of
417 SIMS analysis (Fig. 8d–f). Mann-Whitney U test calculations (Appendix D) revealed that the
418 correlation between Co and $\delta^{34}S$ is significant at a 5% level of significance (P=0.048,
419 R^2=0.49; Fig. 8g) but Ni is decoupled from $\delta^{34}S$ (R^2=0.12, Fig. 8h).

6. Discussion

421   Primary, seafloor and prograde sulfides provide an insight on the inputs of sulfur to
422 subduction zones, while sulfides associated with the onset of exhumation, provide a record of
423 fluid composition released from the slab. Primary sulfide grains occur as polyhedral blebs
424 with concave inward boundaries (Seyler et al., 2007; Schwarzenbach et al., 2012), a textural
425 characteristic not observed in the samples presented here. In addition, none of the sulfides
426 analysed in this study have $\delta^{34}S$ values of ~0 ‰, and therefore sulfur is not solely mantle
427 derived (e.g., Alt and Shanks, 1998; Sakai et al., 1984; Shanks et al., 1995). Instead, the
428 samples from Serra di Pigno and Capu Corvoli record a wide range of sulfur isotopic
429 concentrations from 1.7–15.5 ‰. On the basis of textural observations and non-zero $\delta^{34}S$
430 values, it is concluded that primary sulfides are not preserved in the studied samples.

431   Serra di Pigno samples proximal to metasediments and metagabbros (CO13-33 and
432 CO13-55) display different trends in changes to $\delta^{34}S$ values throughout the subduction cycle.
433 The sample in close proximity to metagabbro and calcareous schist (CO13-55, section 4.2.3)
434 shows a significantly different composition for the late sulfides (5.5–8.0‰) compared to
435 earlier sulfides (1.9 to 6.5‰, Fig. 3c). However, there is no significant difference between
436 prograde and retrograde sulfide grains in CO13-33 (Fig. 3b). The $\delta^{34}S$ values of sulfides in
437 CO13-55 are also significantly lower than the sample distal to other lithologies (p=1.81x10$^-$
438 ^{5}), with values of 1.9–8.0‰ and 4.3 to 10.4‰, respectively (Fig. 3a and c). Capu Corvoli
439 chlorite schist and talc schist samples, that are proximal to metagabbro and only metres apart
440 from each other, show very different $\delta^{34}S$ values; CO14-03 has heterogeneous sulfur isotope
441 compositions ranging from 5.9 to 15.5‰, whereas CO14-04 has lower and more
442 homogeneous $\delta^{34}S$ values of 3.6 to 5.4‰ (Fig. 3d and e).

443   The isotopic compositions of the sulfides are assessed in the context of trace element
444 composition, bacterial sulfate reduction, hydrothermal sulfate reduction, sulfur speciation in

16

445 the fluid, rock buffering versus fluid buffering of the samples, the effects temperature during
446 prograde metamorphism, and the effect of lithological mixing.

6.1. Trace element relationships with δ^{34}S

448   Trace element mapping was carried out to determine the relationship between δ^{34}S
449 and trace elements, which provide insights into fluid pathways and potential composition
450 (e.g., Evans et al., 2014; Giacommetti et al., 2014). Whereas no significant correlation was
451 observed between Co or Ni and δ^{34}S in CO14-03 (R^2 = 0.30 and 0.12, respectively) or Ni in
452 CO14-04 (R^2=0.23), the correlation between Co and δ^{34}S in CO14-04 was found to be
453 statistically significant at a 95% confidence level (P=0.048). Therefore, in general δ^{34}S is
454 inferred to be decoupled from Ni and Co, with the exception of Co in CO14-04. The limited
455 data available here, therefore, suggests that trace elements are not controlled by the same
456 processes that determine the S isotope compositions in the pyrite grains. With the exception
457 of Co in CO14-04, the lack of correlation between trace element zoning and δ^{34}S values is in
458 agreement with previous studies on subducted sulfides (Giacommetti et al., 2014), although
459 some correlation between Co and δ^{34}S was reported for pyrites in mafic and sedimentary
460 rocks (Evans et al., 2014; Giacommetti et al., 2014). However, due to the restrictions of the
461 beam size for analysis, it was not possible to assess the δ^{34}S zonation on the <5 μm scale of
462 the Co and Ni zoning, so small length scale variations in S isotope compositions would have
463 been obscured by the relatively large beam size (10 μm).

464   Similarly, it was not possible to determine relationships between trace element
465 concentrations and sulfur isotope compositions in pentlandite grains due to the small size of
466 the grains analysed, so areas selected for analysis were considered to be homogeneous in Co,
467 Ni and As.

6.2. The effect of seafloor processes on sulfur geochemistry

469   The infiltration of sulfate-bearing seawater into mantle peridotite and consequent
470 serpentinisation results in the addition of seawater-derived sulfur to the rock (Alt and Shanks,
471 1998; Delacour et al., 2008). In the case of Alpine Corsica, it is considered that primary
472 mantle rocks were exposed on the seafloor and juxtaposed with the continental basement
473 during Tethyan rifting in the Middle to Late Jurassic (Bathonian to Oxfordian) in an ultra-
474 slow spreading centre or an ocean-continent transition setting (e.g., Vitale Brovarone et al.,
475 2011; 2013). During this time, seawater sulfate had δ^{34}S values of ~ 17‰ (Kampschulte and
476 Strauss, 2004). Hydrothermal alteration may also occur during initial subduction associated

17

477 with slab bending (Ranero and Sallares, 2004). The heterogeneity of δ^{34}S values in both the
478 Serra di Pigno samples (with an overall range from 3.1 to 8.9‰) and the Capu Corvoli
479 samples (3.6 to 15.5‰) implies that seawater sulfate was likely incorporated into the sulfides,
480 and subsequent processes, including bacterial or hydrothermal sulfate reduction on the
481 seafloor, and further fluid:rock interaction during subduction and exhumation, led to a loss of
482 ^{34}S relative to ^{32}S

6.2.1 Bacterial sulfate reduction

484 Hydrogen and CH_4 released during seafloor serpentinisation, provides an energy source
485 for sulfate reducing micro-organisms (e.g., Alt and Shanks, 1998; Schrenk et al., 2004;
486 Kelley et al., 2005; Brazelton et al., 2006; Schwarzenbach et al., 2012, Schrenk et al., 2013
487 and references therein). Bacterial sulfate reduction (BSR) enriches the light isotope in the
488 mineral products, therefore if BSR occurred during serpentinisation in an open system,
489 negative δ^{34}S are expected (e.g., Schwarzenbach et al., 2012). Such a signal is not observed in
490 the sulfides measured here. However, in a closed system, where there is limited fluid
491 circulation, such as in deep sections of magma poor rifted margins (i.e., an ocean-continent
492 transition zone, the proposed pre-subduction geodynamic setting of Alpine Corsica), BSR
493 could enrich ^{34}S over precursor mantle values if the conversion of seawater sulfate to sulfide
494 were close to completion. Nevertheless, if sulfides produced by microbial sulfate reduction
495 were preserved, at least a few negative isotopic values would be expected as most sulfides
496 would have grown in an open system, but this is not the case, therefore BSR is not thought to
497 have played a significant role in the production of the sulfur isotope compositions of the
498 samples described here.

6.2.2 Hydrothermal sulfate reduction

500 Recent studies have shown that Δ^{33}S in addition to δ^{34}S values can be used to
501 distinguish between open or closed system sulfate reduction, and hydrothermal versus
502 bacterial sulfate reduction (Ono et al., 2012; Schwarzenbach et al., 2018). Δ^{33}S values in the
503 samples analysed here indicate a small but significant mass-independent fractionation (MIF)
504 in three pentlandite grains from CO13-40, four pentlandite grains from CO13-55 and three
505 pyrite grains in CO14-04. The data were carefully checked for any variations caused by a
506 drop in S counts or beam centring, and the effects of crystallographic orientation on Δ^{33}S
507 values is considered to be negligible (LaFlamme et al., 2016). Therefore, the Δ^{33}S values are
508 concluded to result from MIF, whereby variation in isotope abundance is not dependent on

18

509   mass and thus records other processes. Insignificant $\Delta^{33}S$ values in most grains is probably a

510   matter of precision. The maximum recorded $\Delta^{33}S$ values for peridotite from the Iberian

511   Margin are 0.14–0.16‰ (Ono et al., 2012; Schwarzenbach et al. 2018), whereas in this study

512    $\Delta^{33}S$ values in pentlandite grains are 0.33–0.67‰ and pyrite grains record $\Delta^{33}S$ values of

513   between -0.17 and +0.11‰. Therefore, the pyrite and pentlandite measurements are less

514   precise but within error of the measurements in Ono et al. (2012) and Schwarzenbach et al.

515   (2018). Lower $\Delta^{33}S$ values in pyrite may be consistent with HSR in an open system, which

516   typically produce more negative $\Delta^{33}S$ values. More precise measurements of $\Delta^{33}S$ are

517   possible using bulk powders and mineral separates (Ono et al., 2012), but not with the *in-situ*

518   SIMS technique used in this study, required for analysis of the small grains in the samples

519   presented here.

520   With the exception of one grain (CO13-55 a2 s1-1), pentlandite grains with

521   significant $\Delta^{33}S$ values are associated with prograde metamorphism and thus hydrothermal

522   sulfate reduction occurred either during seafloor alteration or prograde metamorphism. In

523   contrast, non-zero pyrite $\Delta^{33}S$ values are found in both early and late pyrite. It has been

524   proposed that a MIF-derived signal could result from the breakdown or formation of S^{3-},

525   which could be present in fluids at depth in subduction zones in supercritical fluids

526   (Pokrovski and Dubessy, 2015). Pokrovski and Dubessy (2015) proposed that the S^{3-} effect

527   on MIF could result from its radical properties and resemblance to ozone (O_3). It is possible

528   that the MIF signal reflects either HSR or mineral S^{3-} fractionation or a combination. For

529   example, sulfate could have been hydrothermally reduced on the seafloor, and S^{3-} further

530   could contribute to the MIF signal during subduction. At present, the lack of fractionation

531   factors for the S^{3-} ion prevents a more detailed interpretation of the data.

6.3. The effects of temperature increase associated with prograde metamorphism

533   Temperature influences isotopic re-equilibration, fractionation factors and rates of

534   diffusion during metamorphism (e.g., Bachinski, 1969; Ohmoto and Rye, 1979; Ohmoto and

535   Lasaga, 1982). The effect of temperature on $\delta^{34}S$ depends on the speciation of sulfur. Sulfur

536   is generally considered to be present as mineral-hosted S^-, S^{2-}, S^0 and sulfate (S^{6+}) in

537   serpentinites (e.g., Alt et al., 2013; Debret et al., 2017; Merkulova et al., 2017). The effect of

538   temperature on ^{34}S fractionation between fluid and sulfide minerals is greater for oxidised

539   sulfur (SO_2 and SO_4^{2-}) than reduced sulfur (H_2S and HS^-). The speciation of aqueous sulfur

540   in ultramafic rocks under prograde conditions is poorly constrained, though H_2S (e.g., Peretti

19

et al., 1992), SO_2 or SO_4^{2-} (e.g., Debret et al., 2016) are the most likely species. As discussed above, the S^{3-} ion has also been proposed to be present in high-pressure fluids such as those attributed to subduction zones (Pokrovski and Dubessy, 2015, Section 6.2.2).

The oxide and sulfide assemblages in the Serra di Pigno serpentinites and the prograde assemblage of CO14-04 from Capu Corvoli are low variance and are therefore inferred to be rock buffered with respect to sulfur, with low fluid:rock interaction and hence only local fluid flow. Activity-activity diagrams of oxide and sulfide stability as a function of aO_2 and aS_2 at high pressure (2 GPa, 555ºC) are presented in Evans et al. (2017). The prograde mineral assemblage in the serpentinites analysed (CO13-33, CO13-40 and CO13-55) is serpentine + pentlandite + magnetite ± pyrite, serpentine + pentlandite + magnetite ± heazlewoodite and in the hybrid sample, CO14-04, is talc + chlorite + magnetite + pyrite + pyrrhotite. According to calculated O_2 and S_2 activities associated with subduction (Evans et al., 2017), the oxide and sulfide assemblages present in the rock samples in this study are consistent with relatively low aO_2 and aS_2, therefore, reduced species such as H_2S or HS^- are inferred to be in solution.

Calculations were undertaken to assess the possible effect of isotope fractionation between sulfur hosted in the minerals and sulfur hosted in the fluids as an effect of prograde metamorphism. A minimum temperature of 250ºC was chosen to maximise the calculated effect of fractionation. Fractionation was calculated for isotope equilibrium between pyrrhotite of mantle sulfur isotope composition and fluid, pyrite with a nominal hydrothermal isotope composition and fluid, and recrystallized pentlandite and fluid ($\Delta_{pyrrhotite-H_2S}$, $\Delta_{pyrite-H_2S}$ and $\Delta_{pentlandite-H_2S}$, respectively) in closed and open (Rayleigh) systems. A starting composition of 0‰ was chosen for mantle pyrrhotite (Sakai et al., 1984; Shanks et al., 1995; Alt et al., 1998). Pyrrhotite was included in calculations because it is present in the hybrid samples (see section 3.2). 8‰ was chosen as the starting composition for hydrothermal pyrite, the average of pyrite isotopic analyses here. The value of 6.7‰ for the recrystallised pentlandite was taken from the average analyses of the pentlandite grains in the Serra di Pigno samples. There are currently no fluid-mineral isotope fractionation factors available for pentlandite, so it is assumed that fractionation factors would be similar to either violarite ($Fe^{2+}Ni_2S_4$; Li and Liu, 2006) or pyrrhotite (Ohmoto and Rye, 1979), or somewhere in between these two end members. Fractionation at 250 ºC is minor for both violarite (-1.2‰, Li and Liu, 2006) and pyrrhotite (0.1‰, Ohmoto and Rye, 1979). Therefore, $\Delta_{pentlandite-H_2S}$

20

573 would be minimal at temperatures of 250ºC and above, in both the closed and open system

574 calculations (Fig. 10a, b). Likewise, $\Delta_{pyrite-H_2S}$ would also be minor at 250ºC, at 1.5‰

575 (Ohmoto and Rye, 1979). Therefore, fractionation between reduced sulfide species in

576 solution and sulfide minerals would not be a first order control on the sulfur isotope

577 compositions, hence sulfur isotope ratios reflect those in the fluid or sulfide minerals that

578 have undergone seafloor alteration.

6.4. Retention of seafloor $\delta^{34}S$ in prograde sulfides

580 Sulfides texturally related to prograde to peak metamorphism include pentlandite in

581 CO13-40, pn1 in CO13-33, in CO13-55 and py1 and po1 in CO14-04. $\delta^{34}S$ values in CO13-

582 40 and CO13-33 are similar and range from 4.3 to 10.4‰ in CO13-40 and 6.5 to 8.8‰ in

583 CO13-33. Pentlandite2 in CO13-55 has lower values (1.9 to 5.7‰). The positive $\delta^{34}S$ values

584 suggest that sulfur isotope compositions were not significantly affected by seafloor BSR. In

585 addition, the heterogeneous $\delta^{34}S$ values suggest that diffusion rates were too slow to affect

586 sulfur isotope compositions. Peak metamorphic temperatures were ~414 to 470 ºC and high-

587 pressure metamorphism is estimated to have occurred from ~55 to 34 Ma (Ravna et al., 2010,

588 Vitale Brovarone et al., 2011, 2013). At such temperatures and time scale, diffusion of sulfur

589 is predicted to be on the scale of >100 μm (Watson et al., 2009), inconsistent with the

590 observed heterogeneous $\delta^{34}S$ values in the studied sulfides except pyrites in the talc schist

591 sample, CO14-04, which have homogeneous S isotope compositions. However, sharp

592 gradients in Co and Ni concentrations recorded in pyrite grains (Fig. 8b–f), and the

593 metasomatic nature of this sample, suggest that fluid flow and mass transport and re-

594 equilibration via dissolution-precipitation reactions are likely to prevail and solid state

595 diffusion is inferred to be limited (e.g. Putnis, 2002; Putnis and Austrheim 2009). Therefore,

596 the process of HSR during seafloor alteration is the preferred control on sulfur isotope ratios

597 in prograde sulfides.

598 The preservation of sulfur isotope compositions derived from seafloor sulfate reduction is

599 consistent with the conclusions of Alt et al. (2012a) who compared high-pressure

600 serpentinites from the Voltri Massif and seafloor serpentinite considered unaffected by

601 metamorphism from Val Graveglia, and found no difference in content or isotopic

602 composition of sulfur during subduction on a sample scale. Bulk $\delta^{34}S$ values recorded by

603 high-pressure serpentinites from 6.0 to 14.3‰ were suggested to reflect the retention of

21

604 sulfur from seafloor serpentinisation, where seafloor sulfur isotope compositions range from

605 –4 to 9.8‰.

6.5. Sulfides associated with exhumation

607   The similar range of heterogeneous δ^{34}S values of prograde sulfides and sulfides

608 associated with the onset of exhumation in serpentinites CO13-33 and CO13-55 is consistent

609 with the interpretation of early HSR as the dominant control on sulfur isotope compositions,

610 and the formation of exhumation-related sulfides from this sulfur reservoir. However, the

611 homogeneity of δ^{34}S values in talc schist sample CO14-04, and higher δ^{34}S values of up to

612 8.0‰ and 15.5‰ in sulfides associated with advanced stages of exhumation in the

613 serpentinite sample CO13-55 and chlorite schist CO14-03, respectively, suggest that

614 subduction related fluids may have influenced the sulfur isotope composition of these late

615 sulfides.

616   Late sulfide and oxide mineral asssemblages associated with exhumation in the Capu

617 Corvoli samples, CO14-03 and CO14-04 are high variance, and are therefore fluid buffered

618 with respect to sulfur. The presence of the mineral assemblage magnetite + pyrite is attributed

619 to increased aS_2 and aO_2 (Evans et al., 2017), relative to the Serra di Pigno samples, reflecting

620 more oxidising conditions in the hybrid environment. $\Delta_{\text{pyrite-SO}_2}$ and $\Delta_{\text{pyrite-SO}_4^{2-}}$ fractionation

621 was calculated for the open and closed system models (Fig. 10c–f) using fractionation values

622 from Ohmoto and Rye (1979). It is evident that there is greater fractionation between pyrite

623 and SO_4, at ~23‰ (Fig. 10e, f), compared to pyrite and H_2S. Given the relatively texturally

624 late setting of pyrite grains in the hybrid samples (section 3.2), with the exception of the early

625 assemblage in CO14-04 (see 6.1.1), it is inferred that the hybrid samples record fluid

626 buffering during exhumation and that during this time fluid:rock isotope fractionation could

627 have been significant at a minimum temperature of 250 ºC, the temperature at which

628 fractionation was calculated.

6.5.1. The source of heterogeneous δ^{34}S values in the chlorite schist.

630   The sulfur isotope composition of pyrites in CO14-03, with δ^{34}S values of up to 15.5‰,

631 are higher than serpentinite δ^{34}S values, and are consistent with those of pyrites in Zermatt-

632 Saas mafic eclogite samples associated with retrogression to blueschist facies (10.0–16.5‰,

633 Evans et al., 2014, Fig. 11). The heterogeneity of the pyrites in CO14-03 likely reflects the

634 mixing of fluids from different sources, as expected for a hybridised ultramafic/mafic rock.

22

635   Metasomatism and hybridisation of the rock either during seafloor alteration and/or prograde

636   metamorphism, could have contributed sulfur with high δ^{34}S values to the rock (e.g. Alt and

637   Shanks, 2003). Fluid mixing is possibly facilitated during deformation via fluid migration to

638   low pressure zones (e.g., Evans et al., 2014). The similarity of some pyrite sulfur isotope

639   compositions to those of retrogressed pyrites from mafic samples from the Zermatt-Saas

640   provides additional evidence that metasomatic alteration and mixing with the metagabbro

641   contributed oxidised sulfur-bearing fluids.

642   Fluid transport of sulfur on a sample scale or greater in CO14-03 is consistent with the

643   observed high variance mineral assemblage, where the only late opaque minerals observed

644   are large magnetite grains and pyrite, which replace prograde matrix minerals such as

645   chlorite. The shift from magnetite to pyrite growth during late retrogression associated with

646   exhumation records an increase in sulfur activity during this stage. The increase in sulfur

647   activity probably occurred on relatively short time scales, given the aggregate nature of the

648   pyrites in CO14-03, where such a texture suggests rapid growth and inadequate time to form

649   well-defined crystal faces. Large clusters of aggregate pyrites record the highest δ^{34}S values,

650   some of which surround magnetite grains (Fig. 2j). Rapid pyrite growth is likely consistent

651   with a sudden influx of a sulfur-rich and, given the high δ^{34}S values, oxidised fluid at the

652   onset of exhumation. We speculate that sulfate in solution was reduced to H_2S via interaction

653   of sulfate bearing fluids with a pre-existing Fe^{2+}-bearing silicate, whereby Fe^{2+} was the

654   electron donor for sulfate reduction. Fe^{2+}-bearing chlorite, a phase attributed to stability prior

655   to fluid infiltration at the onset of exhumation, is a plausible candidate. The resultant

656   oxidation from Fe^{2+} to Fe^{3+} within chlorite is consistent with the growth of magnetite at this

657   stage. The reaction of H_2S with Fe^{3+} from magnetite, where ferric iron is considered to react

658   faster than ferrous iron with H_2S (Canfield et al., 1992; Ono et al., 2012), may have triggered

659   the rapid growth of pyrite, hence the observed clusters around magnetite.

660   *6.5.2. The source of homogeneous δ^{34}S values in the talc schist.*

661   CO14-04 pyrites record relatively low (4–5‰) and homogeneous δ^{34}S values. The

662   transition from prograde metamorphism to exhumation is associated with a small but

663   significant shift to lower δ^{34}S values in the pyrites. The shift from low to high variance

664   sulfide mineral assemblages associated with this transition records a switch from a rock

665   buffered or closed system to fluid buffered or open system with respect to sulfur. The low

666   variance assemblage associated with prograde metamorphism is consistent with rock

23

667 buffering with H_2S or HS^- in solution. Therefore, in the talc schist sample, it is possible that

668 the infiltration of external fluids homogenised pre-existing heterogeneous $\delta^{34}S$ values that

669 were associated with pre-exhumation stages of metamorphism.

6.6. Implications for sulfur cycling

671   The *in-situ* $\delta^{34}S$ data presented here is consistent with the range of whole rock $\delta^{34}S$

672 values presented in Alt et al. (2012a) from the Voltri Massif in the Ligurian Alps, where the

673 pre-subduction setting is similar to that of the samples studied here (Fig. 11). Alt et al. (2012)

674 proposed that the sulfur isotope compositions of serpentinites remained unaltered during

675 subduction. The *in-situ* technique, however, allows the evolution of $\delta^{34}S$ values to be

676 assessed as a function of the stage of sulfide growth, and provides an insight into fluid:rock

677 interaction. The observation that all sulfides record $\delta^{34}S$ values in between those of the

678 mantle and Jurassic seawater-derived sulfate, suggests that sulfides record mixing between

679 these two end members (Fig. 11). The textural preservation of sulfides with inclusions of

680 antigorite, a high-pressure serpentine polymorph, and the overprinting of late antigorite

681 generations by retrograde sulfides suggest sulfur redistribution on a millimetre scale during

682 subduction. Spatially heterogeneous sulfur isotope compositions, similar chemical

683 compositions of sulfides between early and late sulfides (section 5.1), and low variance

684 mineral assemblages, is consistent with a closed system, and only local scale redistribution of

685 sulfur with low fluid:rock ratios.

686   Sulfides associated with advanced stages of exhumation in serpentinite proximal to

687 metagabbro and calcareous schist (CO13-55), record a significant shift towards higher $\delta^{34}S$

688 values, and record the presence of fluids with the ability to carry oxidised sulfur (SO_2 or

689 SO_4^{2-}) at depth within subduction zones. Fluids bearing oxidised sulfur were most likely

690 devolatilised from lithologies other than serpentinites during subduction, because the sulfide

691 mineral assemblages in the Serra di Pigno serpentinites are consistent with reduced sulfur in

692 solution.

693   The hybrid samples are fluid buffered on at least the scale of the pyrites (0.1 to 1cm)

694 and the homogeneity of the early and late S isotope compositions of pyrite in CO14-04

695 suggests that fluids and therefore sulfur may have been sourced externally, consistent with

696 the metasomatic alteration of this sample. The high variance mineral assemblage of CO14-03

697 is associated with heterogeneous $\delta^{34}S$ values, unlike the homogeneous values in CO14-04.

24

One possibility is that sulfur in this rock derived from both mafic and ultramafic sources, consistent with the hybrid nature of this sample.

The composition of fluids released during dehydration of serpentinites are poorly constrained, however a fluid inclusion study in high-pressure serpentinites from Cima di Gagnone, Swiss Alps, suggests the release of Cl-bearing fluids during the dehydration reactions of chrysotile, and antigorite + brucite (Scambelluri et al., 2004a; Scambelluri et al., 2004b; Kodolányi and Pettke, 2011; Scambelluri et al., 2015). On the basis of the presence of sulfides in the fluid inclusions, sulfur in such fluids is proposed to be hosted by a reduced species (Scambelluri et al., 2015). On the other hand, the low ferric iron contents and high Fe isotopic values of serpentinites have been suggested to record the devolatilisation of sulfate-bearing fluids during subduction (Debret et al., 2016), consistent with the presence of sulfate in seafloor serpentine minerals (Debret et al., 2017). In this study, on the basis of mineral assemblages in the Serra di Pigno serpentinites, the reduced species H_2S or HS^- are inferred to be in solution during subduction.

7. Conclusions

In-situ sulfur isotope data, in combination with textural and trace element compositions provides insights into the processes, evolution of the redox state and source of sulfur in serpentinites and hybrid mafic/ultramafic rocks through the subduction cycle. High $\delta^{34}S$ values were recorded in all sulfides (1.9–15.5‰), where the simplest explanation for this observation is the early fixation and retention of oxidised sulfur from seafloor alteration in the serpentinites. This explanation is consistent with heterogeneous values, low variance mineral assemblage and low degrees of fluid:rock interaction in most serpentinite samples, with the exception of a serpentinite sample proximal to metagabbro and calcareous schist, where there is a marked shift towards higher $\delta^{34}S$ values in pentlandite grains associated with late exhumation. Therefore, in the studied serpentinites, sulfur is redistributed only on a local mm to cm scale throughout the subduction cycle, consistent with the conclusions of previous sulfur isotope studies (e.g., Alt et al., 2012a). Infiltration of slab derived fluids during exhumation affected the sulfur mineral assemblages and sulfur isotope compositions in hybrid samples. Hybridisation of mafic/ultramafic rocks appears to be dominated by fluid-buffered assemblages with high sulfur activities, suggesting mobilisation of oxidised sulfur during 'mixing' of these lithologies on a scale greater than a thin-section sized sample.

25

Acknowledgements

References

Agard, P., & Vitale-Brovarone, A. (2013). Thermal regime of continental subduction: the record from exhumed HP–LT terranes (New Caledonia, Oman, Corsica). *Tectonophysics*, **601**, 206-215.

Alt, J. C., Garrido, C. J., Shanks, W., Turchyn, A., Padrón-Navarta, J. A., Sánchez-Vizcaino, V. L., Pugnaire, M. T. G. & Marchesi, C. (2012b), 'Recycling of water, carbon, and sulfur during subduction of serpentinites: A stable isotope study of Cerro del Almirez, Spain', *Earth and Planetary Science Letters* **327**, 50–60.

Alt, J. C., Shanks, W. C., Bach, W., Paulick, H., Garrido, C. J., & Beaudoin, G. (2007). Hydrothermal alteration and microbial sulfate reduction in peridotite and gabbro exposed by detachment faulting at the Mid- Atlantic Ridge, 15° 20′ N (ODP Leg 209): A sulfur and oxygen isotope study. *Geochemistry, Geophysics, Geosystems*, **8**(8).

Alt, J. C., Shanks, W., Crispini, L., Gaggero, L., Schwarzenbach, E. M., Früh-Green, G. L. & Bernasconi, S. M. (2012a), 'Uptake of carbon and sulfur during seafloor serpentinization and the effects of subduction metamorphism in Ligurian peridotites', *Chemical Geology* **322**, 268–277.

Alt, J. C., Schwarzenbach, E. M., Früh-Green, G. L., Shanks III, W. C., Bernasconi, S. M., Garrido, C. J., ... & Marchesi, C. (2013). The role of serpentinites in cycling of carbon and sulfur: seafloor serpentinization and subduction metamorphism. *Lithos*, *178*, 40-54.

Alt, J. C. & Shanks, W. C. (2003), 'Serpentinization of abyssal peridotites from the MARK area, Mid-Atlantic Ridge: sulfur geochemistry and reaction modeling', *Geochimica et Cosmochimica Acta* **67**(4), 641–653.

Alt, J. C. & Shanks, W. C. (1998), 'Sulfur in serpentinized oceanic peridotites: Serpentinization processes and microbial sulfate reduction', *Journal of Geophysical Research: Solid Earth* **103**(B5), 9917–9929.

Alt, J. C., Shanks, W. C. & Jackson, M. C. (1993), 'Cycling of sulfur in subduction zones: The geochemistry of sulfur in the Mariana Island Arc and back-arc trough', *Earth and Planetary Science Letters* **119**(4), 477–494.

Aulbach, S., Stachel, T., Seitz, H.-M. & Brey, G. P. (2012), 'Chalcophile and siderophile elements in sulfide inclusions in eclogitic diamonds and metal cycling in a Paleoproterozoic subduction zone', *Geochimica et Cosmochimica Acta* **93**, 278–299.

Ault, W. & Jensen, M. (1963), 'Summary of sulfur isotope standards.', *In: Biogeochemistry of Sulfur Isotopes.Jensen ML (ed) Nat Sci Found, Symp Proc, Yale University*.

Bach, W., Garrido, C. J., Paulick, H., Harvey, J., & Rosner, M. (2004). Seawater- peridotite interactions: First insights from ODP Leg 209, MAR 15 N. *Geochemistry, Geophysics, Geosystems*, *5*(9).

Bachinski, D. J. (1969). Bond strength and sulfur isotopic fractionation in coexisting sulfides. *Economic Geology*, *64*(1), 56-65.

Barnes, S. J. (2000), 'Chromite in komatiites, II. Modification during greenschist to mid-amphibolite facies metamorphism', *Journal of Petrology* **41**(3), 387–409.

Barnes, S. J. & Roeder, P. L. (2001), 'The range of spinel compositions in terrestrial mafic and ultramafic rocks', *Journal of Petrology* **42**(12), 2279–2302.

Barnes, S. J., Heggie, G. J. & Fiorentini, M. L. (2013), 'Spatial variation in platinum group element concentrations in ore-bearing komatiite at the Long-Victor deposit, Kambalda Dome, Western Australia: enlarging the footprint of nickel sulfide orebodies', *Economic Geology* **108**(5), 913–933.

Bearden, J.A. (1964) "X-ray Wavelengths", Report NYO 10586, U.S. Atomic Energy Commission, Oak Ridge, Tennessee.

Bliss, N. & MacLean, W. (1975), 'The paragenesis of zoned chromite from central Manitoba',

Geochimica et Cosmochimica Acta **39**(6), 973–990.

Brazelton, W. J., Schrenk, M. O., Kelley, D. S. & Baross, J. A. (2006), 'Methane-and sulfur-metabolizing microbial communities dominate the Lost City hydrothermal field ecosystem', *Applied and Environmental Microbiology* **72**(9), 6257–6270.

Canfield D. E., Raiswell R. and Bottrell S. (1992) The reactivity of sedimentary iron minerals toward sulfide. Am. J. Sci. 292, 659-659.

Colás, V.; González-Jiménez, J. M.; Griffin, W. L.; Fanlo, I.; Gervilla, F.; O'Reilly, S. Y.; Pearson, N. J.; Kerestedjian, T. & Proenza, J. A. (2014), 'Fingerprints of metamorphism in chromite: New insights from minor and trace elements', *Chemical Geology* **389**, 137–152.

Crossley, R. J., Evans, K. A., Reddy, S. M., & Lester, G. W. (2017). Redistribution of Iron and Titanium in High- Pressure Ultramafic Rocks. *Geochemistry, Geophysics, Geosystems*, *18*(11), 3869-3890.

Debret, B., Andreani, M., Mucoz, M., Bolfan-Casanova, N., Carlut, J., Nicollet, C., Schwartz, S. & Trcera, N. (2014), 'Evolution of Fe redox state in serpentine during subduction', *Earth and Planetary Science Letters* **400**, 206–218.

Debret, B., Millet, M.-A., Pons, M.-L., Bouilhol, P., Inglis, E. & Williams, H. (2016), 'Isotopic evidence for iron mobility during subduction', *Geology* **44**(3), 215–218.

Debret, B., & Sverjensky, D. A. (2017). Highly oxidising fluids generated during serpentinite breakdown in subduction zones. *Scientific reports*, *7*(1), 10351.

Delacour, A., Früh-Green, G. L., Bernasconi, S. M. & Kelley, D. S. (2008), 'Sulfur in peridotites and gabbros at Lost City (30 N, MAR): Implications for hydrothermal alteration and microbial activity during serpentinization', *Geochimica et Cosmochimica Acta* **72**(20), 5090–5110.

Donovan, J. J., Kremser, D., & Fournelle, J. H. (2012). Probe for EPMA: acquisition, automation and analysis. *Probe Software, Inc., Eugene, Oregon.*

Duncumb, P. and Reed, S.J.B. (1968) *In:* Quantitative Electron Probe Microanalysis (K.F.J. Heinrich, ed.), Nat. Bureau Stand. Spl. Publ. **298**, 133.

Duncumb, P. and Shields, P.K. (1966) *In*: The Electron Microprobe (T.D. McKinley, K.F.J. Heinrich and D.B. Wittry, eds.), Wiley: New York, p. 284.

28

Ernst, W.G. & Liu, J., 1998. Experimental phase-equilibrium study of Al- and Ti-contents of calcic amphibole in MORB – a semiquantitative thermobarometer. *American Mineralogist*, **83**, 952–969.

Evans, B. W. & Frost, B. R. (1975), 'Chrome-spinel in progressive metamorphism—a preliminary analysis', *Geochimica et Cosmochimica Acta* **39**(6-7), 959–972.

Evans, B. W., & Kuehner, S. M. (2011). A nickel-iron analogue of balangeroite and gageite (Sasaguri, Kyushu, Japan). *European Journal of Mineralogy*, **23**(5), 717-720.

Evans, K. A. (2006). Redox decoupling and redox budgets: Conceptual tools for the study of earth systems. *Geology*, **34**(6), 489-492.

Evans, K. (2012), 'The redox budget of subduction zones', *Earth-Science Reviews* **113**(1), 11–32.

Evans, K. A., & Powell, R. (2015). The effect of subduction on the sulfur, carbon and redox budget of lithospheric mantle. *Journal of Metamorphic Geology*, **33**(6), 649-670.

Evans, K. A., Reddy, S. M., Tomkins, A. G., Crossley, R. J., & Frost, B. R. (2017). Effects of geodynamic setting on the redox state of fluids released by subducted mantle lithosphere. *Lithos*, **278**, 26-42.

Evans, K., Tomkins, A., Cliff, J. & Fiorentini, M. (2014), 'Insights into subduction zone sulfur recycling from isotopic analysis of eclogite-hosted sulfides', *Chemical Geology* **365**, 1–19.

Farquhar, J., Cliff, J., Zerkle, A. L., Kamyshny, A., Poulton, S. W., Claire, M., Adams, D. & Harms, B. (2013), 'Pathways for Neoarchean pyrite formation constrained by mass-independent sulfur isotopes', *Proceedings of the National Academy of Sciences* **110**(44), 17638–17643.

Faure, M. & Malavieille, J. (1981), 'Etude structurale d'un cisallement ductile: le charriage ophiolitique Corse dans la région de Bastia.', *Bulletin de la Societe Geologique de France, 23*.

Frost, B. R. (1991), 'Stability of oxide minerals in metamorphic rocks', *Reviews in Mineralogy and Geochemistry* **25**(1), 469–488.

Gervilla, F.; Padrón-Navarta, J.; Kerestedjian, T.; Sergeeva, I.; González-Jiménez, J. & Fanlo, I. (2012), 'Formation of ferrian chromite in podiform chromitites from the Golyamo

Kamenyane serpentinite, Eastern Rhodopes, SE Bulgaria: a two-stage process', *Contributions to Mineralogy and Petrology* **164**(4), 643–657.

Giacometti, F., Evans, K. A., Rebay, G., Cliff, J., Tomkins, A. G., Rossetti, P., Vaggelli, G. & Adams, D. T. (2014), 'Sulfur isotope evolution in sulfide ores from Western Alps: Assessing the influence of subduction-related metamorphism', *Geochemistry, Geophysics, Geosystems* **15**(10), 3808–3829.

Grieco, G. & Merlini, A. (2012), 'Chromite alteration processes within Vourinos ophiolite', *International Journal of Earth Sciences* **101**(6), 1523–1533.

Groppo, C., & Compagnoni, R. (2007). Metamorphic veins from the serpentinites of the Piemonte Zone, western Alps, Italy: a review. *Periodico di Mineralogia*, *76*, 127-153.

Harris, L., 1985. Progressive and polyphase deformation of the Schistes Lustrés in Cap Corse, Alpine Corsica. *Journal of Structural Geology* **7**, 637-650.

Heinrich, K.F.J. (1969) National Bureau of Standards, Technical Note 521.

Heinrich, K.F.J. (1986) *In:* Proc. 11th Intl. Conf. on X-ray Optics and Microanalysis (J.D. Brown and R.H. Packwood, eds.), Univ. Western Ontario, London, Ont. Canada, p. 67.

Ishihara, S. & Sasaki, A. (1989), 'Sulfur isotopic ratios of the magnetite-series and ilmenite-series granitoids of the Sierra Nevada batholith—a reconnaissance study', *Geology* **17**(9), 788–791.

Kampschulte, A. & Strauss, H. (2004), 'The sulfur isotopic evolution of Phanerozoic seawater based on the analysis of structurally substituted sulfate in carbonates', *Chemical Geology* **204**(3), 255–286.

Kelley, D. S., Karson, J. A., Früh-Green, G. L., Yoerger, D. R., Shank, T. M., Butterfield, D. A., Hayes, J. M., Schrenk, M. O., Olson, E. J., Proskurowski, G. & others (2005), 'A serpentinite-hosted ecosystem: the Lost City hydrothermal field', *Science* **307**(5714), 1428–1434.

Kimball, K. L. (1990), 'Effects of hydrothermal alteration on the compositions of chromian spinels', *Contributions to Mineralogy and Petrology* **105**(3), 337–346.

Kodolányi, J. & Pettke, T. (2011), 'Loss of trace elements from serpentinites during fluid-assisted transformation of chrysotile to antigorite—An example from Guatemala', *Chemical Geology* **284**(3), 351–362.

30

Labidi, J., Cartigny, P., Hamelin, C., Moreira, M., & Dosso, L. (2014). Sulfur isotope budget (32 S, 33 S, 34 S and 36 S) in Pacific–Antarctic ridge basalts: A record of mantle source heterogeneity and hydrothermal sulfide assimilation. *Geochimica et Cosmochimica Acta*, *133*, 47-67.

LaFlamme, C., Martin, L., Jeon, H., Reddy, Steven, M., Selvaraja, V., Caruso, S., Bui, Hao, T., Roberts, M. P., Voute, F., Hagemann, S., Wacey, D., Wing, B., Fiorentini, M. & Kilburn, M. R. (2016), 'In situ multiple sulfur isotope analysis by SIMS of pyrrhotite, pentlandite and chalcopyrite to refine magmatic ore genetic models', *Chemical Geology* **444**, 1–15.

Lahondère, D. & Guerrot, C. (1997), 'Datation Nd-Sm du métamorphisme éclogitique en Corse alpine: un argument pour l'existence, au Crétacé supérieur, d'une zone de subduction active localisée le long du block corse-sarde.', *Géologie de la France* **3**, 3-11.

Lahondère, J.; Lahondère, D.; Lluch, D.; Ohnenstetter, M.; Dominici, R. & Vautralle, C. (1992), 'Carte géologique de la France a 1/50000', *Luri, BRGM*.

Laird, J., & Albee, A. L. (1981). Pressure, temperature, and time indicators in mafic schist; their application to reconstructing the polymetamorphic history of Vermont. *American Journal of Science*, *281*(2), 127-175.

Li, X. P., Rahn, M., & Bucher, K. (2004). Serpentinites of the Zermatt- Saas ophiolite complex and their texture evolution. *Journal of Metamorphic Geology*, **22**(3), 159-177.

Li, Y. & Liu, J. (2006), 'Calculation of sulfur isotope fractionation in sulfides', *Geochimica et Cosmochimica Acta* **70**(7), 1789–1795.

Magott, R.; Fabbri, O. & Fournier, M. (2016), 'Subduction zone intermediate-depth seismicity: Insights from the structural analysis of Alpine high-pressure ophiolite-hosted pseudotachylyte (Corsica, France)', *Journal of Structural Geology* **87**, 95–114.

Marschall, H. R. & Shimizu, N. (2012), 'Sulfur Isotopes in High-Pressure Rocks', *Mineralogical Magazine* **76(6)**, 2070.

Marschall, H. R., & Schumacher, J. C. (2012). Arc magmas sourced from mélange diapirs in subduction zones. *Nature Geoscience*, **5**, 862–867.

Mattauer, M.; Faure, M. & Malavieille, J. (1981), 'Transverse lineation and large-scale structures related to Alpine obduction in Corsica', *Journal of Structural Geology* **3**(4), 401–409.

Mattauer, M.; Proust, F. & Etchecopar, A. (1977), 'Lineation "a" et mecanisme de cisaillement simple lie au chevauchement de la nappe des schistes lustres en Corse', *Bulletin de la Société Géologique de France* **7**(4), 841–847.

Mellini, M.; Rumori, C. & Viti, C. (2005), 'Hydrothermally reset magmatic spinels in retrograde serpentinites: formation of "ferritchromit" rims and chlorite aureoles', *Contributions to Mineralogy and Petrology* **149**(3), 266–275.

Meresse, F., Lagabrielle, Y., Malavieille, J., & Ildefonse, B. (2012). A fossil Ocean–Continent Transition of the Mesozoic Tethys preserved in the Schistes Lustrés nappe of northern Corsica. *Tectonophysics*, **579**, 4-16.

Merkulova, M. V., Muñoz, M., Brunet, F., Vidal, O., Hattori, K., Vantelon, D., ... & Huthwelker, T. (2017). Experimental insight into redox transfer by iron-and sulfur-bearing serpentinite dehydration in subduction zones. *Earth and Planetary Science Letters*, *479*, 133-143.

Merlini, A.; Grieco, G. & Diella, V. (2009), 'Ferritchromite and chromian-chlorite formation in mélange-hosted Kalkan chromitite (Southern Urals, Russia)', *American Mineralogist* **94**(10), 1459–1467.

Miller, J. A., & Cartwright, I. (2006). Albite vein formation during exhumation of high- pressure terranes: a case study from alpine Corsica. *Journal of Metamorphic Geology*, **24**(5), 409-428.

Mukherjee, R.; Mondal, S. K.; Rosing, M. T. & Frei, R. (2010), 'Compositional variations in the Mesoarchean chromites of the Nuggihalli schist belt, Western Dharwar Craton (India): potential parental melts and implications for tectonic setting', *Contributions to Mineralogy and Petrology* **160**(6), 865–885.

Mungall, J. E. (2002). Roasting the mantle: Slab melting and the genesis of major Au and Au-rich Cu deposits. *Geology*, *30*(10), 915-918.

Ohmoto, H. & Lasaga, A. C. (1982), 'Kinetics of reactions between aqueous sulfates and sulfides in hydrothermal systems', *Geochimica et Cosmochimica Acta* **46**(10), 1727–1745.

Ohmoto, H. & Rye, R. (1979), 'Isotopes of sulfur and carbon. Geochemistry of Hydrothermal Ore Deposits (Barnes, HL, ed.), 509-567', John Wiley & Sons Inc., New York.

Ono, S., Keller, N. S., Rouxel, O. & Alt, J. C. (2012), 'Sulfur-33 constraints on the origin of

secondary pyrite in altered oceanic basement', *Geochimica et Cosmochimica Acta* **87**, 323–340.

Padrón-Navarta, J. A., Sánchez-Vizcaíno, V. L., Hermann, J., Connolly, J. A., Garrido, C. J., Gómez-Pugnaire, M. T., & Marchesi, C. (2013). Tschermak's substitution in antigorite and consequences for phase relations and water liberation in high-grade serpentinites. *Lithos*, **178**, 186-196.

Paytan, A., Kastner, M., Campbell, D., & Thiemens, M. H. (1998). Sulfur isotopic composition of Cenozoic seawater sulfate. *Science*, **282**(5393), 1459-1462.

Paytan, A., Kastner, M., Campbell, D., & Thiemens, M. H. (2004). Seawater sulfur isotope fluctuations in the Cretaceous. *science*, *304*(5677), 1663-1665.

Peretti, A., Dubessy, J., Mullis, J., Frost, B. R. & Trommsdorff, V. (1992), 'Highly reducing conditions during Alpine metamorphism of the Malenco peridotite (Sondrio, northern Italy) indicated by mineral paragenesis and H2 in fluid inclusions', *Contributions to Mineralogy and Petrology* **112**(2-3), 329–340.

Peters, M., Strauss, H., Farquhar, J., Ockert, C., Eickmann, B., & Jost, C. L. (2010). Sulfur cycling at the Mid-Atlantic Ridge: A multiple sulfur isotope approach. *Chemical Geology*, *269*(3-4), 180-196.

Philibert, J. (1963) In Proc. 34th Intl. Symp. X-ray Optics and X-ray Microanalysis, Stanford University (H.H. Pattee, V.E. Cosslett and A. Engstrom, eds.) Academic Press: New York, p. 379.

Pokrovski, G. S. & Dubessy, J. (2015), 'Stability and abundance of the trisulfur radical ion in hydrothermal fluids', *Earth and Planetary Science Letters* **411**, 298–309.

Putnis A (2002) Mineral replacement reactions: from macroscopic observations to microscopic mechanisms, Mineralogical Magazine, **66**, 689–708.

Putnis, A., & Austrheim, H. (2010). Fluid- induced processes: metasomatism and metamorphism. *Geofluids*, **10**(1- 2), 254-269.

Ranero, C. & Sallares, V. (2004), 'Geophysical evidence for hydration of the crust and mantle of the Nazca plate during bending at the north Chile trench', *Geology* **32**(7), 549–552.

Ravna, E., Andersen, T. B., Jolivet, L. & De Capitani, C. (2010), 'Cold subduction and the

formation of lawsonite eclogite–constraints from prograde evolution of eclogitized pillow lava from Corsica', *Journal of Metamorphic Geology* **28**(4), 381–395.

Reed, S. J. B. (1965). Characteristic fluorescence corrections in electron-probe microanalysis. *British Journal of Applied Physics*, **16**(7), 913.

Rees, C., Jenkins, W. & Monster, J. (1978), 'The sulfur isotopic composition of ocean water sulfate', *Geochimica et Cosmochimica Acta* **42**(4), 377–381.

Richards, J. P. (2015). The oxidation state, and sulfur and Cu contents of arc magmas: implications for metallogeny. *Lithos*, **233**, 27-45.

Sakai, H., Des Marais, D., Ueda, A. & Moore, J. (1984), 'Concentrations and isotope ratios of carbon, nitrogen and sulfur in ocean-floor basalts', *Geochimica et Cosmochimica Acta* **48**(12), 2433–2441.

Santiago Ramos, D., Shimizu, N. & Scambelluri, M. (2012), Sulfur isotopic variations during subduction of hydrated lithosphere: the Erro Tobbio case, *in* 'AGU Fall Meeting Abstracts', pp. 04.

Scambelluri, M., Fiebig, J., Malaspina, N., Müntener, O. & Pettke, T. (2004b), 'Serpentinite subduction: implications for fluid processes and trace-element recycling', *International Geology Review* **46**(7), 595–613.

Scambelluri, M., Müntener, O., Ottolini, L., Pettke, T. T. & Vannucci, R. (2004a), 'The fate of B, Cl and Li in the subducted oceanic mantle and in the antigorite breakdown fluids', *Earth and Planetary Science Letters* **222**(1), 217–234.

Scambelluri, M.; Pettke, T.; Rampone, E.; Godard, M. & Reusser, E. (2014), 'Petrology and trace element budgets of high-pressure peridotites indicate subduction dehydration of serpentinized mantle (Cima di Gagnone, Central Alps, Switzerland)', *Journal of Petrology*, **55**(3), 459–498.

Scambelluri, M., Pettke, T. & Cannaт, E. (2015), 'Fluid-related inclusions in Alpine high-pressure peridotite reveal trace element recycling during subduction-zone dehydration of serpentinized mantle (Cima di Gagnone, Swiss Alps)', *Earth and Planetary Science Letters* **429**, 45–59.

Schrenk, M., Kelley, D., Bolton, S. & Barossa, J. (2004) Low archaeal diversity linked to subseafloor geochemical processes at the Lost City Hydrothermal Flield, Mid-Atlantic Ridge. Environmental Microbiology, **6**, 1086–1095.

Schrenk, M. O., Brazelton, W. J., & Lang, S. Q. (2013). Serpentinization, carbon, and deep life. *Reviews in Mineralogy and Geochemistry*, **75**(1), 575-606.

Schwarzenbach, E. M., Früh-Green, G. L., Bernasconi, S. M., Alt, J. C., Shanks III, W. C., Gaggero, L., & Crispini, L. (2012). Sulfur geochemistry of peridotite-hosted hydrothermal systems: comparing the Ligurian ophiolites with oceanic serpentinites. *Geochimica et Cosmochimica Acta*, *91*, 283-305.

Schwarzenbach, E. M., Gill, B. C., & Johnston, D. T. (2018). Unraveling multiple phases of sulfur cycling during the alteration of ancient ultramafic oceanic lithosphere. *Geochimica et Cosmochimica Acta*, *223*, 279-299.

Seal, R. R. (2006), 'Sulfur isotope geochemistry of sulfide minerals', *Reviews in mineralogy and geochemistry* **61**(1), 633–677.

Seyler, M., Lorand, J. P., Dick, H. J., & Drouin, M. (2007). Pervasive melt percolation reactions in ultra-depleted refractory harzburgites at the Mid-Atlantic Ridge, 15 20′ N: ODP Hole 1274A. *Contributions to Mineralogy and Petrology*, **153**(3), 303.

Shanks, W., Bцhlke, J. & Seal, R. (1995), 'Stable Isotopes in Mid-Ocean Ridge Hydrothermal Systems: Interactions Between Fluids, Minerals, and Organisms', *Seafloor Hydrothermal Systems: Physical, Chemical, Biological, and Geological Interactions*, 194–221.

Shanks, W., Bischoff, J. L. & Rosenbauer, R. J. (1981), 'Seawater sulfate reduction and sulfur isotope fractionation in basaltic systems: interaction of seawater with fayalite and magnetite at 200–350 C', *Geochimica et Cosmochimica Acta* **45**(11), 1977–1995.

Shimizu N, Scambelluri M, S. R. D. &. T. S. (2013), 'Boron and Sulfur Isotopic Variations during Subduction of Hydrated Lithosphere: The Erro Tobbio Case', *Mineralogical Magazine* **77(5)**, 2201.

Spandler, C., Hermann, J., Faure, K., Mavrogenes, J. A. & Arculus, R. J. (2008), 'The importance of talc and chlorite "hybrid" rocks for volatile recycling through subduction zones, evidence from the high-pressure subduction mélange of New Caledonia', *Contributions to Mineralogy and Petrology* **155**(2), 181–198.

Spandler, C., & Pirard, C. (2013). Element recycling from subducting slabs to arc crust: A review. *Lithos*, **170**, 208-223.

Spear, F.S., 1981. An experimental study of hornblende stability and compositional variability in amphibolite. *American Journal of Science,* **281**, 697–734.

Tostevin, R., Turchyn, A. V., Farquhar, J., Johnston, D. T., Eldridge, D. L., Bishop, J. K. & McIlvin, M. (2014), 'Multiple sulfur isotope constraints on the modern sulfur cycle', *Earth and planetary science letters* **396**, 14–21.

Ueda, A. & Sakai, H. (1984), 'Sulfur isotope study of Quaternary volcanic rocks from the Japanese Islands Arc', *Geochimica et Cosmochimica Acta* **48**(9), 1837–1848.

Vitale Brovarone, A., Beltrando, M., Malavieille, J., Giuntoli, F., Tondella, E., Groppo, C., Beyssac, O. & Compagnoni, R. (2011), 'Inherited ocean–continent transition zones in deeply subducted terranes: insights from Alpine Corsica', *Lithos* **124**(3), 273–290.

Vitale Brovarone, A., Beyssac, O., Malavieille, J., Molli, G., Beltrando, M. & Compagnoni, R. (2013), 'Stacking and metamorphism of continuous segments of subducted lithosphere in a high-pressure wedge: the example of Alpine Corsica (France)', *Earth-Science Reviews* **116**, 35–56.

Vitale Brovarone, A. & Herwartz, D. (2013), 'Timing of HP metamorphism in the Schistes Lustrés of Alpine Corsica: New Lu–Hf garnet and lawsonite ages', *Lithos* **172**, 175–191.

Wacey, D., Kilburn, M. R., Saunders, M., Cliff, J. & Brasier, M. D. (2011), 'Microfossils of sulfur-metabolizing cells in 3.4-billion-year-old rocks of Western Australia', *Nature Geoscience* **4**(10), 698–702.

Wallace, P. J. & Edmonds, M. (2011), 'The sulfur budget in magmas: evidence from melt inclusions, submarine glasses, and volcanic gas emissions', *Reviews in Mineralogy and Geochemistry* **73**(1), 215–246.

Warburton, J., 1986. The ophiolite-bearing Schistes Lustrés nappe in Alpine Corsica: A model for the emplacement of ophiolites that have suffered HP/LP metamorphism. In: Blueschists and Eclogites (B.W. Evans and E.H. Brown, eds). *Geological Society of America Memoir*, **164**, 313-331.

Watson, E. B., Cherniak, D. J., & Frank, E. A. (2009). Retention of biosignatures and mass-independent fractionations in pyrite: Self-diffusion of sulfur. *Geochimica et Cosmochimica Acta*, **73**(16), 4792-4802.

Wylie, A. G.; Candela, P. A. & Burke, T. M. (1987), 'Compositional zoning in unusual Zn-rich chromite from the Sykesville District of Maryland and its bearing on the origin of" ferritchromit"', *American Mineralogist* **72**(3-4), 413–422.

36

Figure Captions

Figure 1: (a) map showing the locations and P-T conditions of the field areas Serra di Pigno and Capu Corvoli on Cap Corse, Corsica (redrawn from Brovarone et al., 2011, 2013). Abbreviations correspond to the name of the units; Mm: Monte Maggiore peridotite unit, Ce: Centuri continental slice, Ma: Macinaggio flysch, Fa: Farinole continental slice, Ne: Nebbio unit; Te: Tenda unit. **(b)** map of Serra di Pigno sample localities. **(c)** map of Capu Corvoli sample localities (adapted from Lahondère, 1992). MB = metabasalt, CS = calcareous schist, H = hybrid, MG = metagabbro. **(d)** Field photo showing the juxtaposition of lithologies at Serra di Pigno. **(e)** Field photo of the contact between metagabbro and chlorite schist at Capu Corvoli.

Figure 2: microphotographs illustrating key textures, bse = backscattered electron, rfl = reflected light and xpl = cross-polarised light image. **Serra di Pigno serpentinite samples:** (a) rfl: pentlandite grain in CO13-40 with early antigorite inclusions (atg1) replacement by atg2. (b) rfl: pentlandite (pn1) in CO13-33 aligned with atg1 foliation. (c) rfl: pn2 overprints early Cr- rich spinel grains in CO13-33. (d) rfl: pn3 grains in CO13-33 cross-cut late antigorite and associated with magnetite (mt2) (e) bse: pn1 cross-cut by atg3 in CO13-55 (f) xpl: pn2 associated with atg2 in CO13-55 (f) rfl: pn2 associated with atg2 in CO13-55 (h) xpl: euhedral grain of pn3 associated with late atg3 veins in CO13-55. **Capu Corvoli hybrid samples**: (i) rfl: pyrite grains within matrix in chlorite schist CO14-03. (j) pyrite rims on magnetite, and pyrite connected to the matrix by fractures in magnetite in chlorite schist CO14-03. (k) rfl: py1 grains in talc schist CO14-04 with inclusions of chromite and an iron hydroxide rim, which contains inclusions of po. (l) xpl: py2 grains with a talc2 rim in talc schist CO14-04 (xpl).

Figure 3: Histograms of δ^{34}S values in sulfides for (a) CO13-40, (b) CO13-33, (c) CO13-55, (d) CO14-03 and (e) CO14-04. Red/no lines= sulfide grains related to prograde and peak metamorphism. Blue/horizontal lines = sulfide grains related to early exhumation. Green/diagonal lines = sulfide grains related to late exhumation.

Figure 4: CO13-40. Reflected light images of pentlandite grains (a) s1 in area 3, (b) s8 in area 3, (c) s2 in area 1, (d) s9 + repeated analysis (r) in area 3 and (e) s3 in area 3. (f) NanoSIMS map of grain s3 in area 3, circle indicates point of SIMS analysis. All values are

δ^{34}S (‰) unless otherwise indicated. **Figure 1:** CO13-33. Reflected light images of pentlandite grains (a) Pn1 grain s14 in area 3, (b) Pn2 grain s4 in area 2, (c) Pn2 grain s3 in area 2, (d) Pn3 grain s10 in area 2 and (e) Pn3 grain s10 in area 3. (f) Co map (wt%) of a pn2 grain. All values are δ^{34}S (‰).

Figure 5: CO13-33. Reflected light images of pentlandite grains (a) Pn1 grain s14 in area 3, (b) Pn2 grain s4 in area 2, (c) Pn2 grain s3 in area 2, (d) Pn3 grain s10 in area 2 and (e) Pn3 grain s10 in area 3. (f) Co map (wt%) of a pn2 grain. All values are δ^{34}S.

Figure 6: CO13-55 pentlandite. (a) bse image of Pn2 grain s2 in area 3. (b) Co map (wt%) of Pn2 grain s1 in area 3. (c) bse image of Pn2 grain s1 in area 2. (d) bse image of Pn3 grain s2 in area 3. (e) bse image of Pn4 grain s3 in area 1. (f) bse image of Pn4 grain s1 in area 1. All values are δ^{34}S (‰).

Figure 7: CO14-03. Reflected light images of gold coated (a) matrix grain within 1mm of magnetite, area 1 analyses 1-8. (b) matrix grain area 2 analyses 9-13 (c) matrix grain area 3 within 1mm of magnetite analyses 9–11. (d) large cluster of pyrite aggregates in matrix area 2 1–8. (e) large cluster of pyrite grains on rim of large magnetite, area 3 analyses 1–11. All values are δ^{34}S (‰).

Figure 8: (a) reflected light image of matrix pyrite grain in CO14-03, area 1 analyses 1-8 for matrix pyrite, the same grain is shown in images b-c; (b) EPMA derived trace element map of Co in pyrite grain in CO14-03; (c) EPMA derived trace element map of Ni; (d) reflected light image of py2 grain s1 in area 1 in CO14-04; the same grain is shown in images e–f; (e) EPMA derived trace element map of Co in pyrite grain in CO14-04 (f) EPMA derived trace element map of Ni in pyrite grain in CO14-04; (g) Ni (wt%) plotted against δ^{34}S in CO14-03 and CO14-04; (h) Co (wt%) plotted against δ^{34}S in CO14-04. The values in b–c and e–f are δ^{34}S (‰). Sample CO14-03 = orange circles and sample CO14-04 = yellow diamonds in g–h.

Figure 9: CO14-04. Reflected light images of gold coated py1 grains (a) s2 in area 2, (b) s3 in area 2, (c) s1 in area 3, (d) s2 in area 3 and py2 grains in (e) s1 in area 1 and (f) s1 in area 2. All values are δ^{34}S (‰).

Figure 10: Fractionation calculation plots of δ^{34}S and progression of the reactions mantle (m) pyrrhotite-H_2S, mantle pentlandite-H_2S, hydrothermally altered and recrystallized (r) pyrrhotite-H_2S, hydrothermally altered and recrystallised (r) pentlandite-H_2S, and hydrothermal pyrite-H_2S for (a) a closed system and (b) open system (Rayleigh) fractionation, between δ^{34}S and progression of the reactions mantle (m) pyrrhotite-SO_2,

mantle pentlandite-SO_2 and hydrothermal pyrite-SO_2 for (c) a closed system and (d) an open system (Rayleigh), and between $\delta^{34}S$ and progression of the reactions mantle (m) pyrrhotite-SO_4^{2-}, mantle pentlandite-SO_4^{2-} and hydrothermal pyrite-SO_4^{2-} for (c) a closed system and (d) an open system (Rayleigh), and between $\delta^{34}S$ and progression of the reactions mantle (m) pyrrhotite-SO_4^{2-}, mantle pentlandite-SO_4^{2-} and hydrothermal pyrite-SO_4^{2-} for (e) a closed system and (f) an open system (Rayleigh).

Figure 11: Comparison of $\delta^{34}S$ values from this study to those from other whole rock and *in-situ* studies.

Figure 1
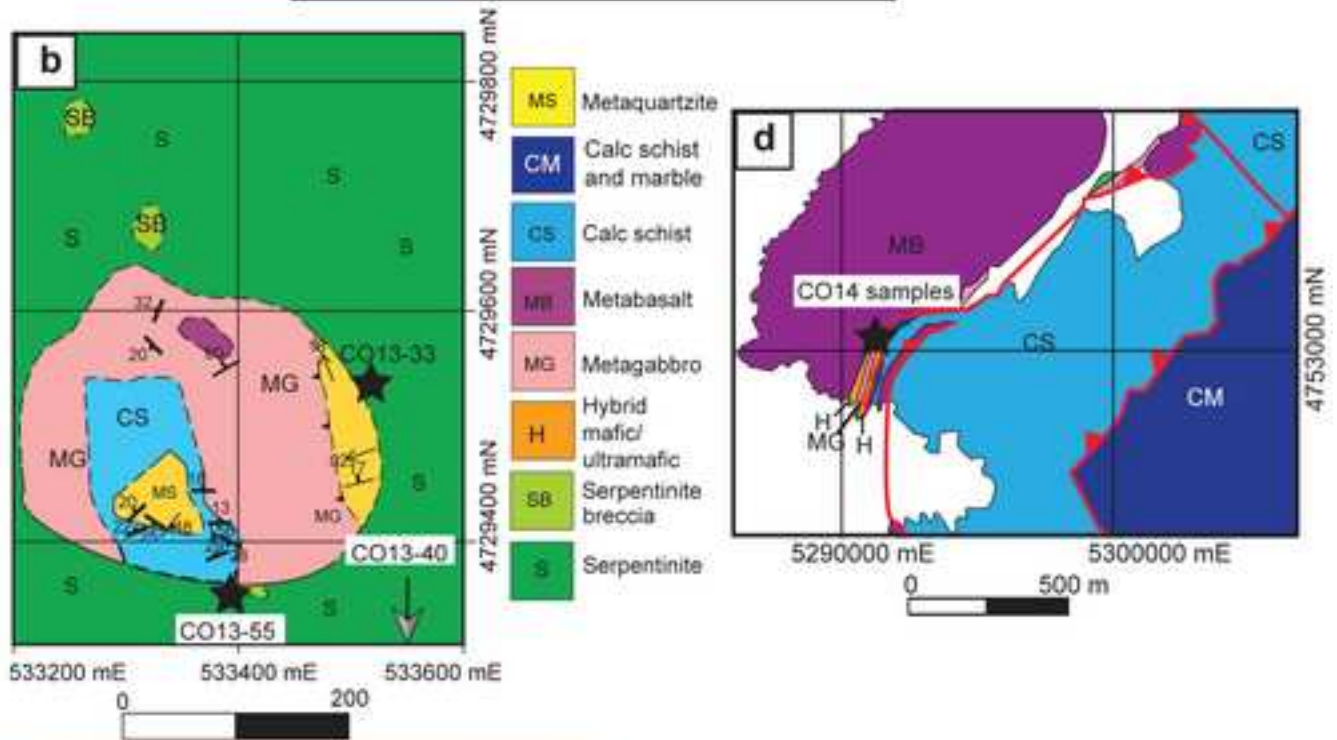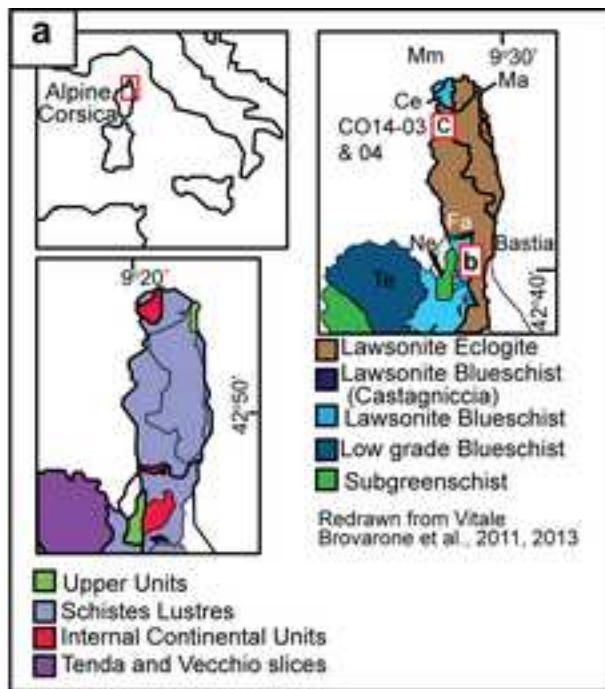
Figure 2
Click here to download high resolution image
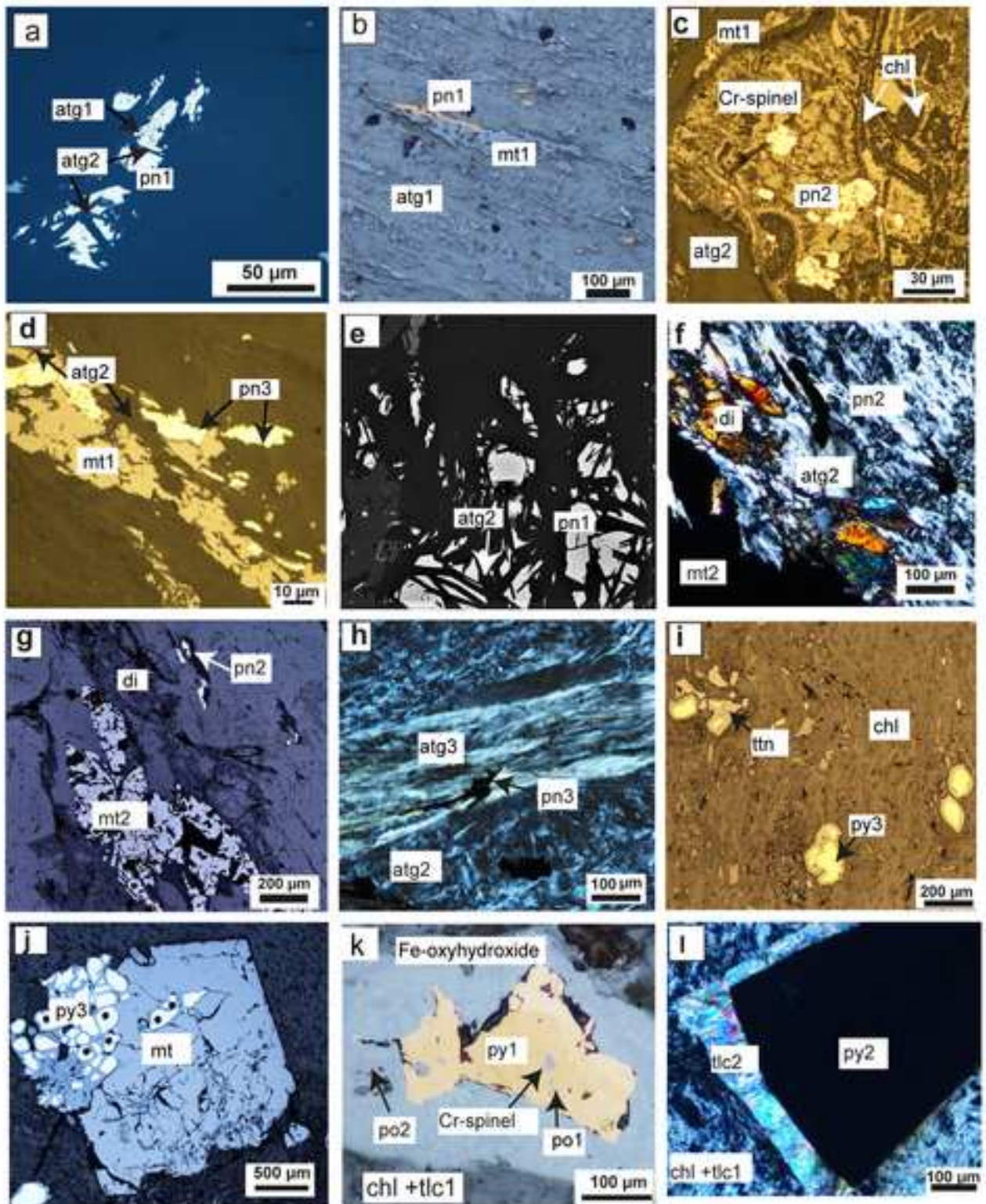
Figure 3
Click here to download high resolution image
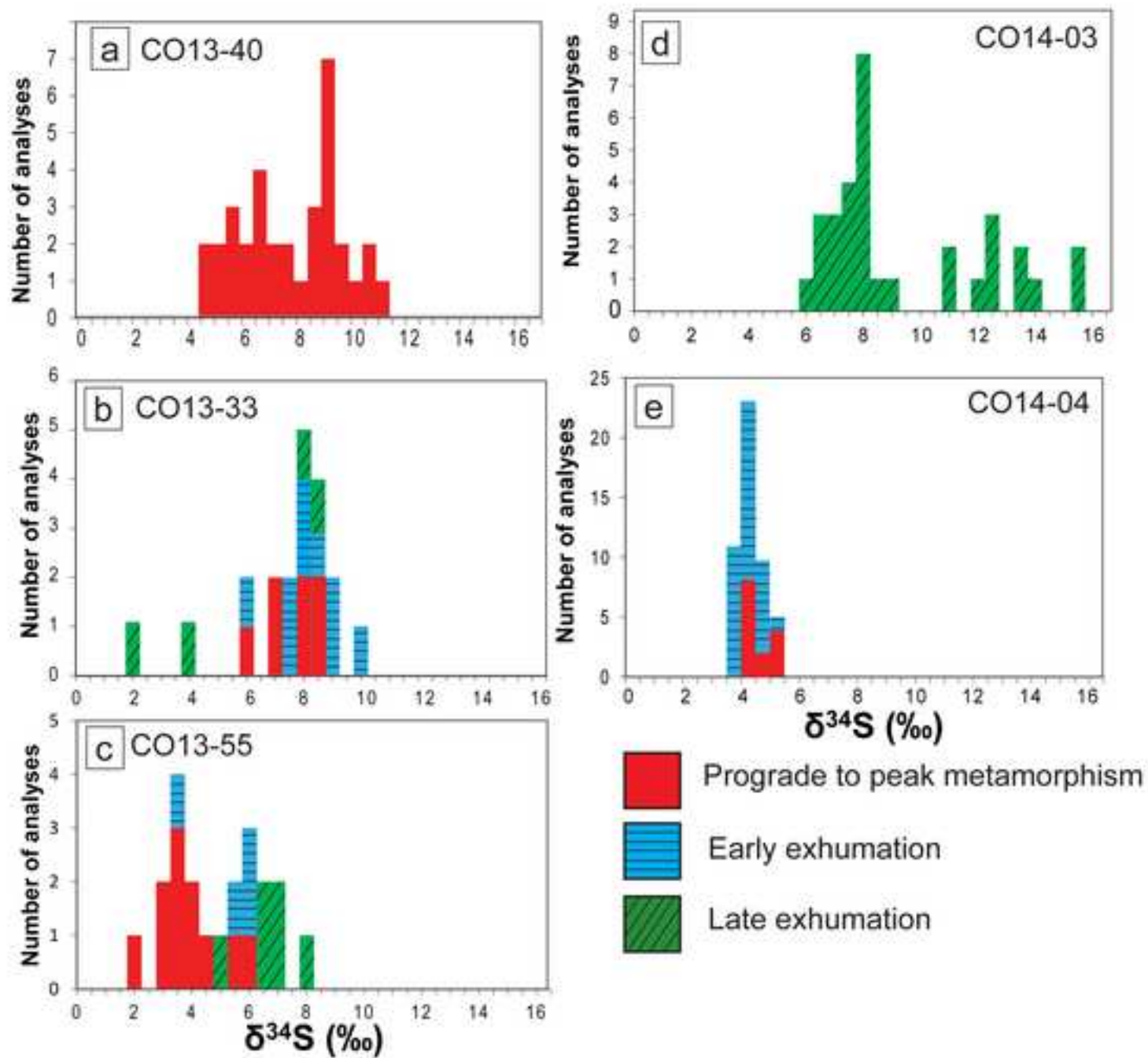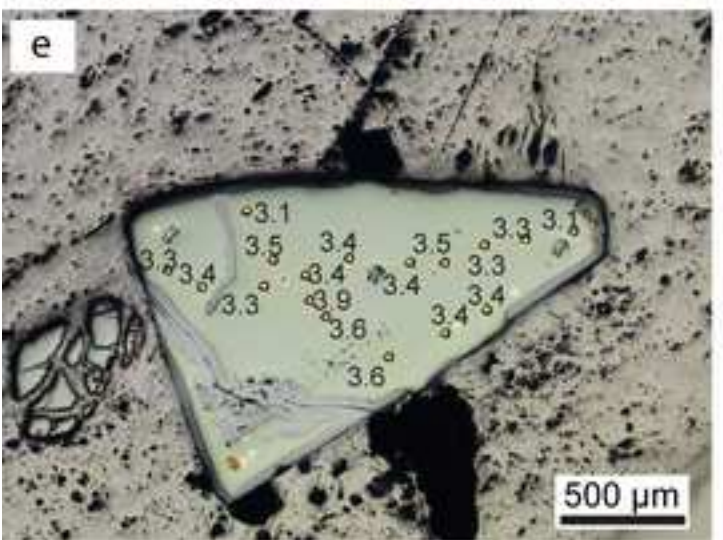
Figure 4
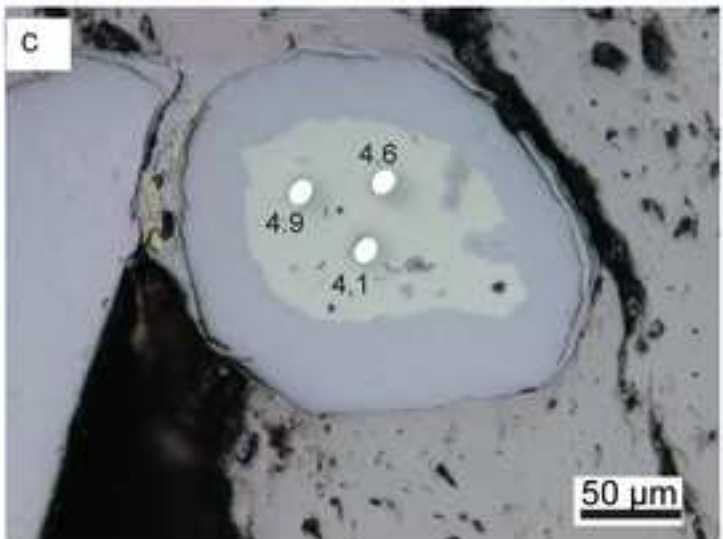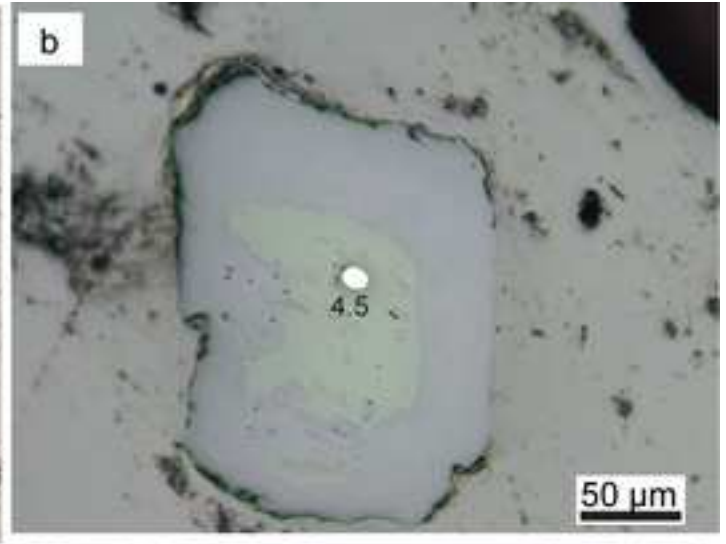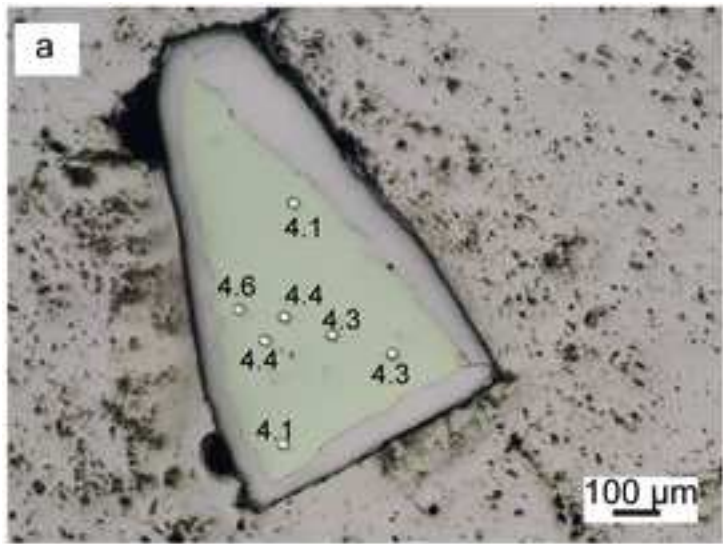**Click here to download high resolution image**
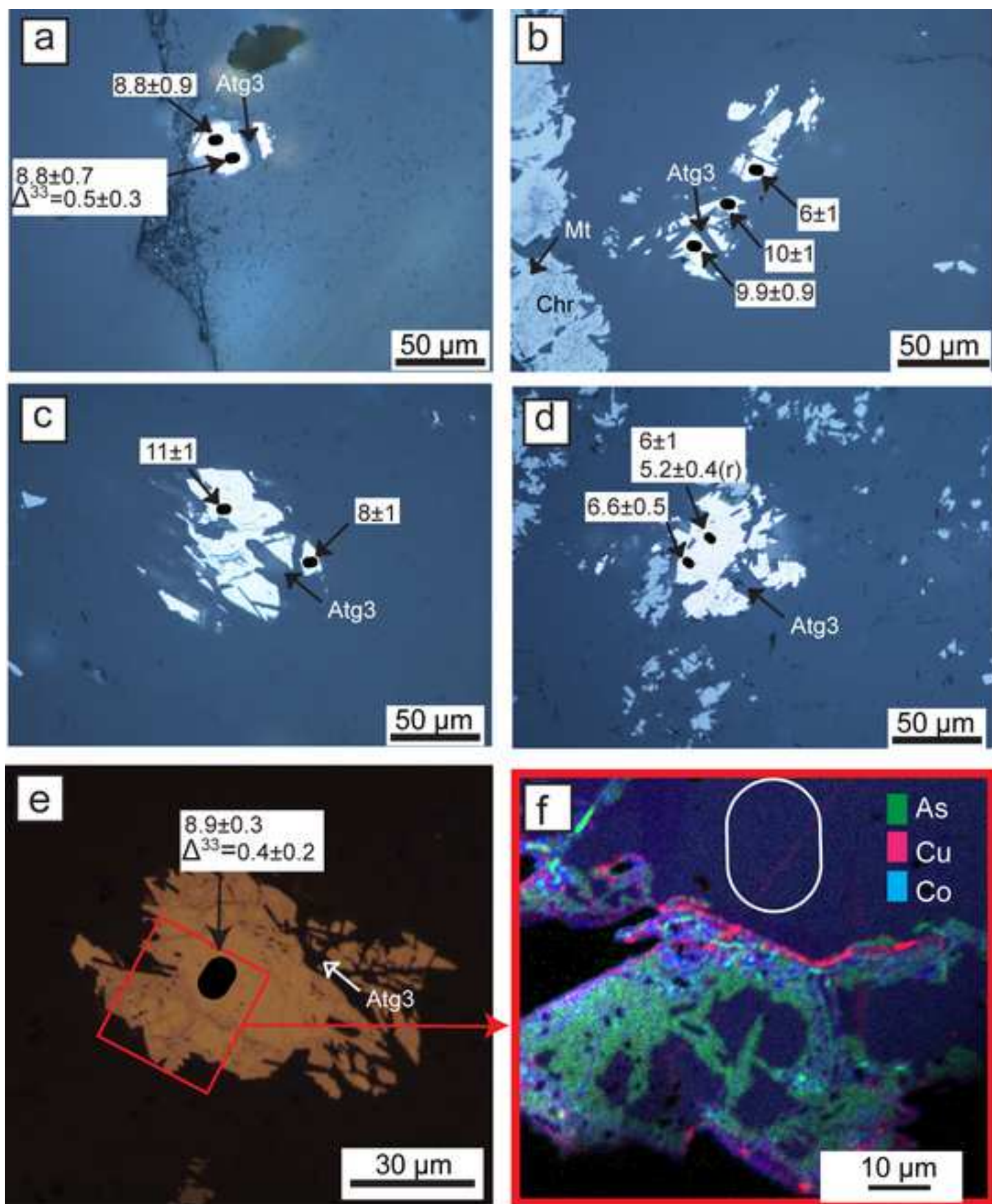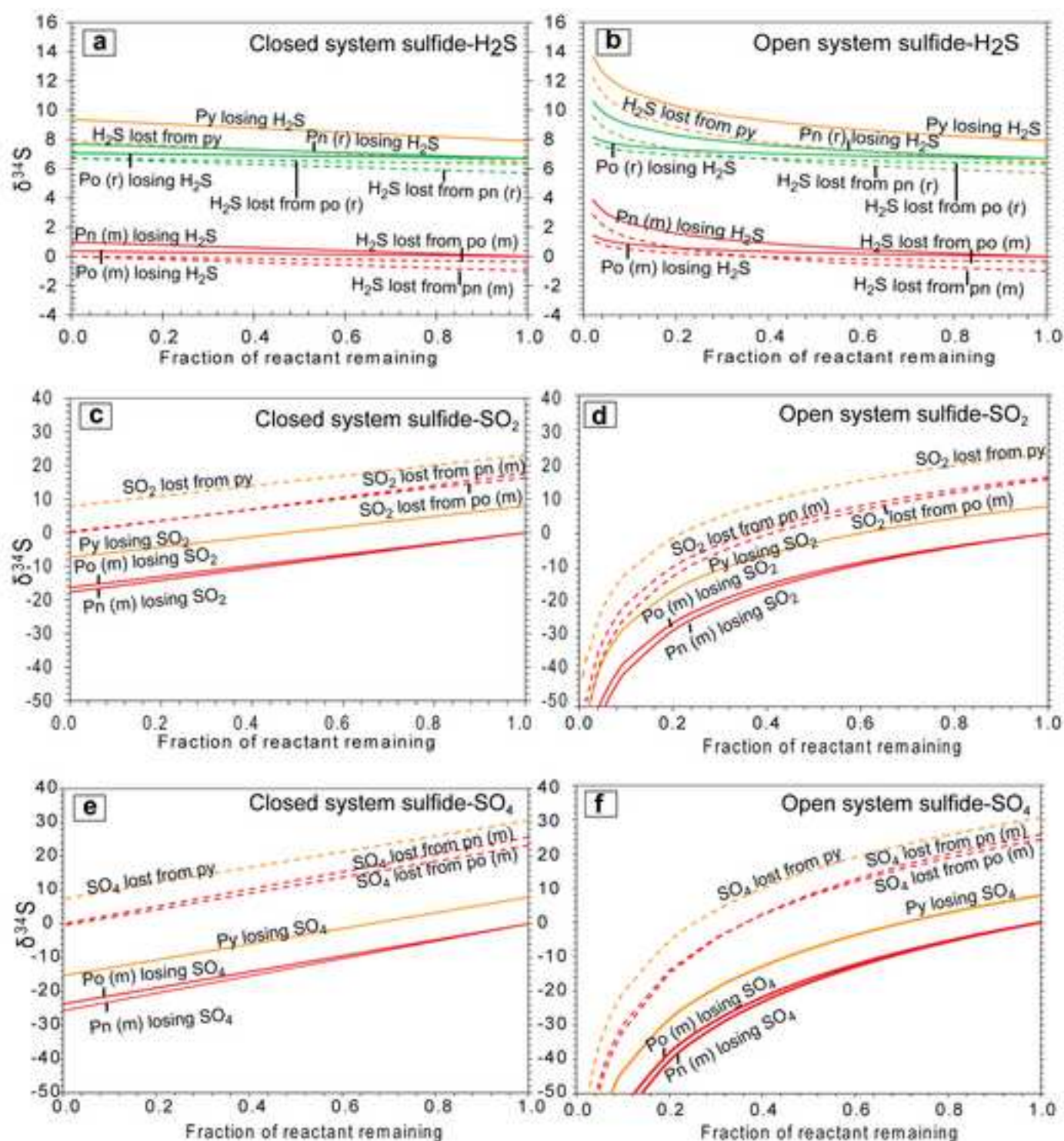
Figure 5
[Click here to download high resolution image](#)
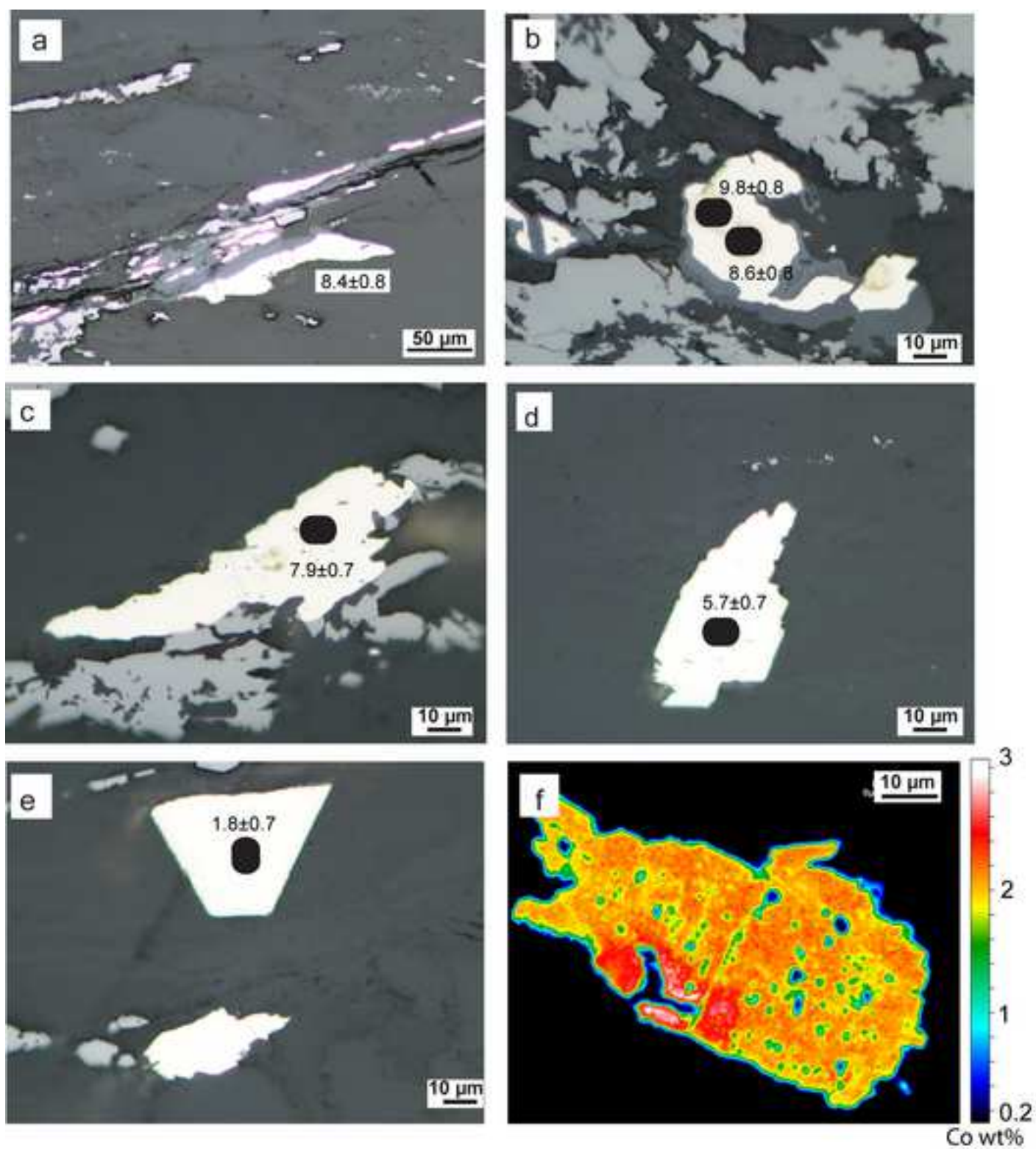
Figure 6
Click here to download high resolution image
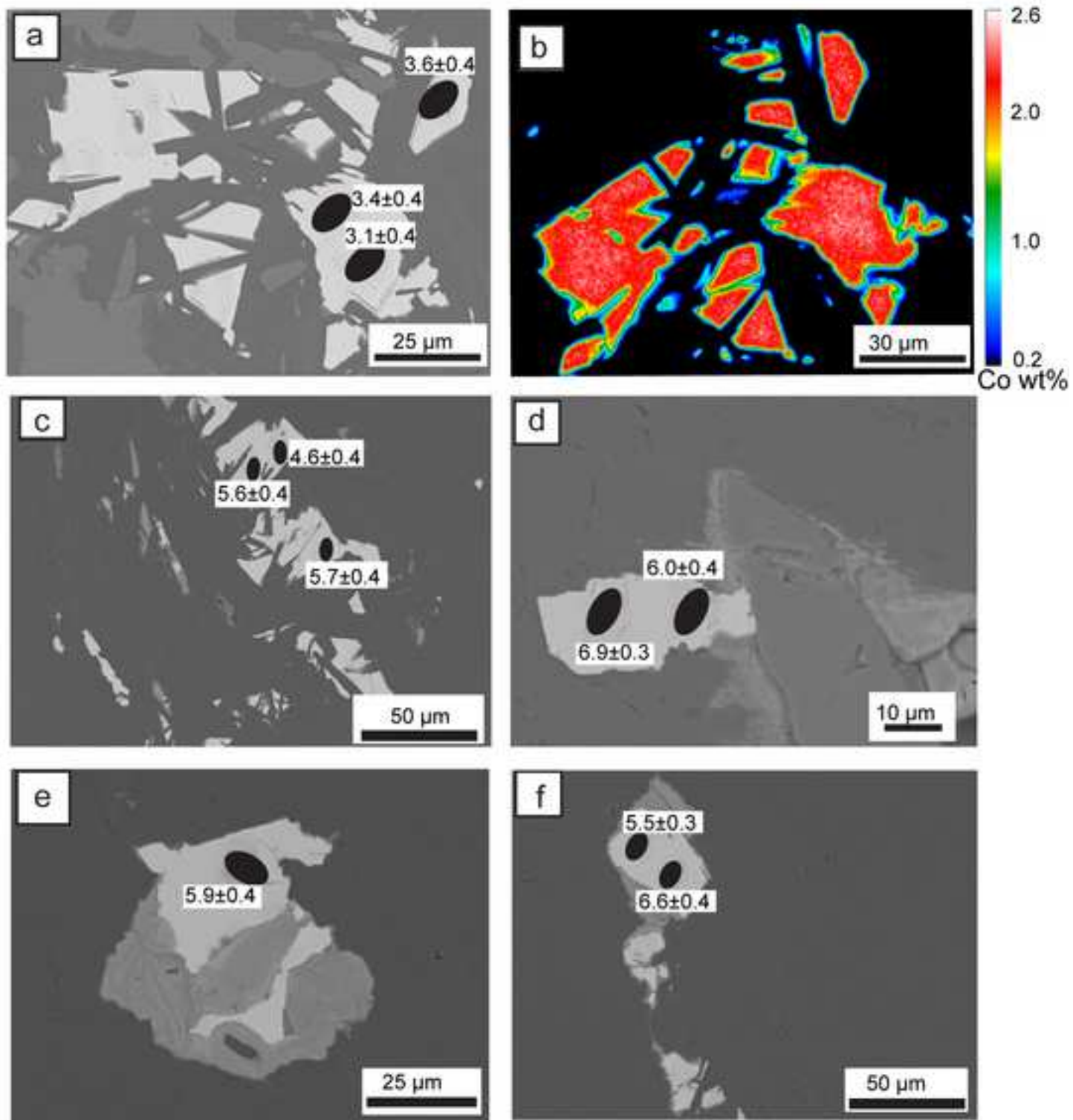
Figure 6

Figure 7
Click here to download high resolution image
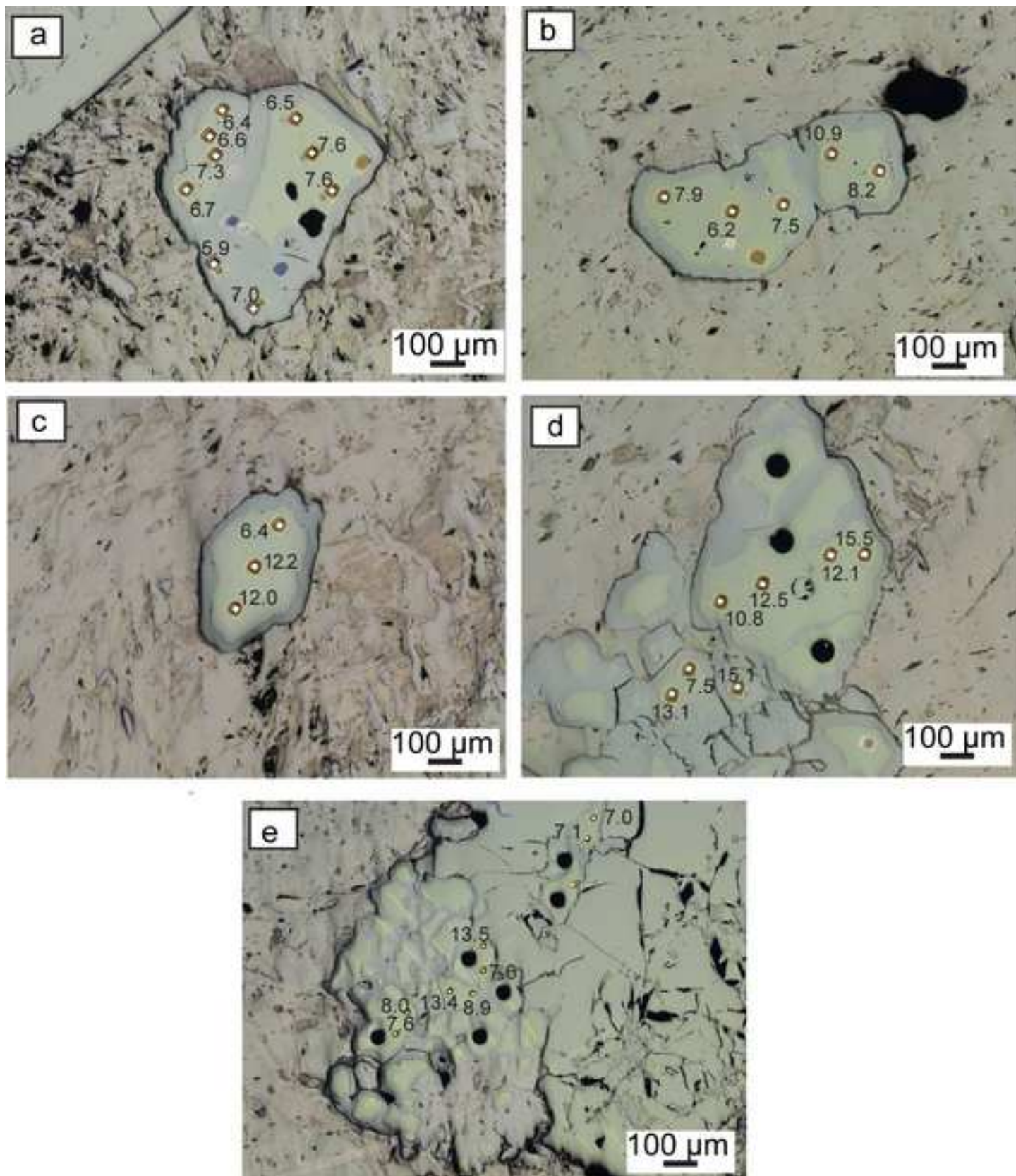
Figure 8
Click here to download high resolution image
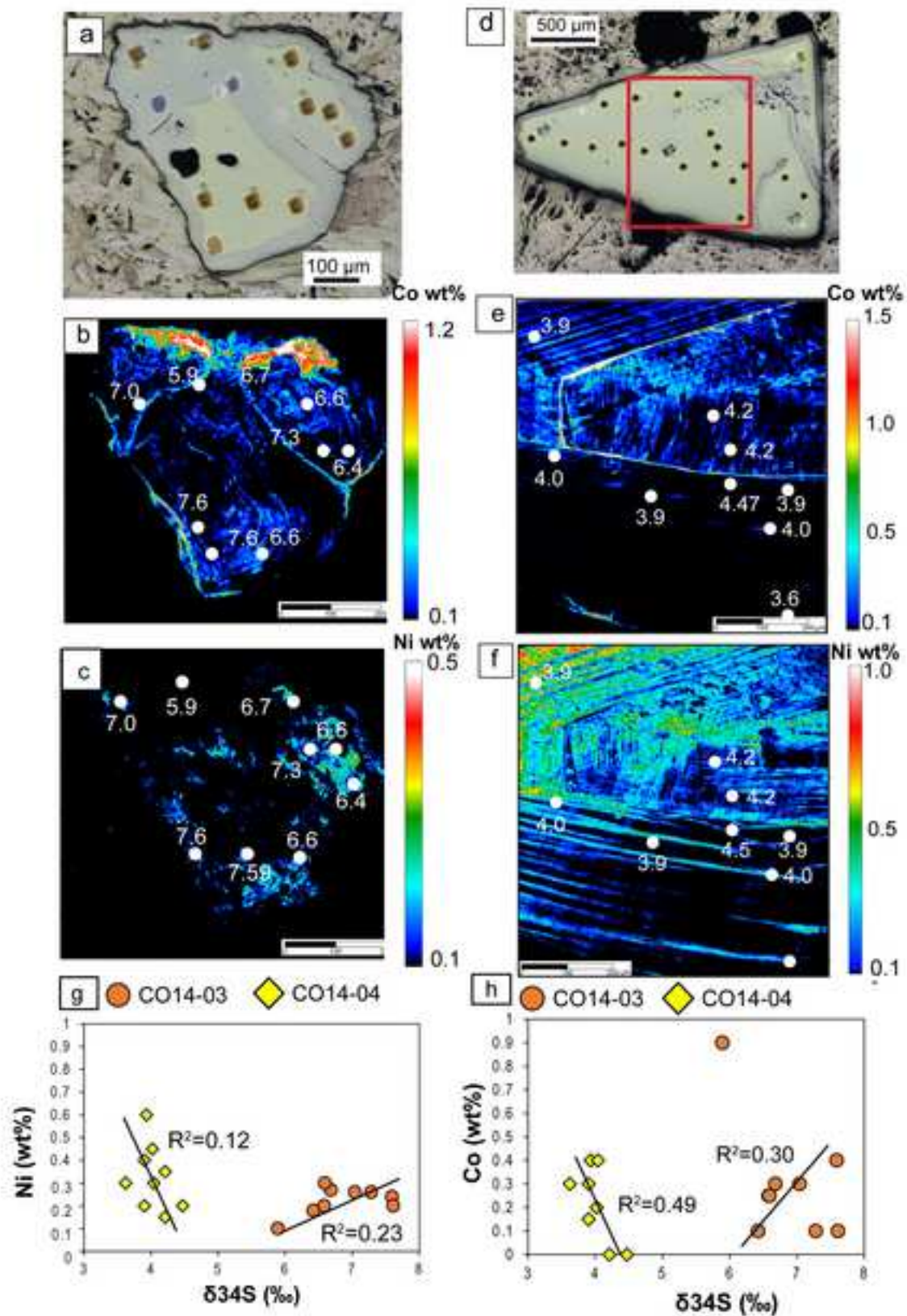
Figure 9
[Click here to download high resolution image](#)
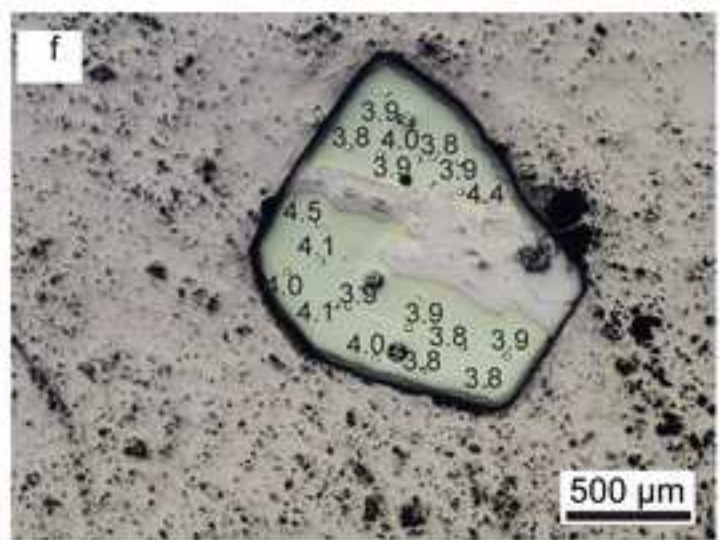
Figure 10
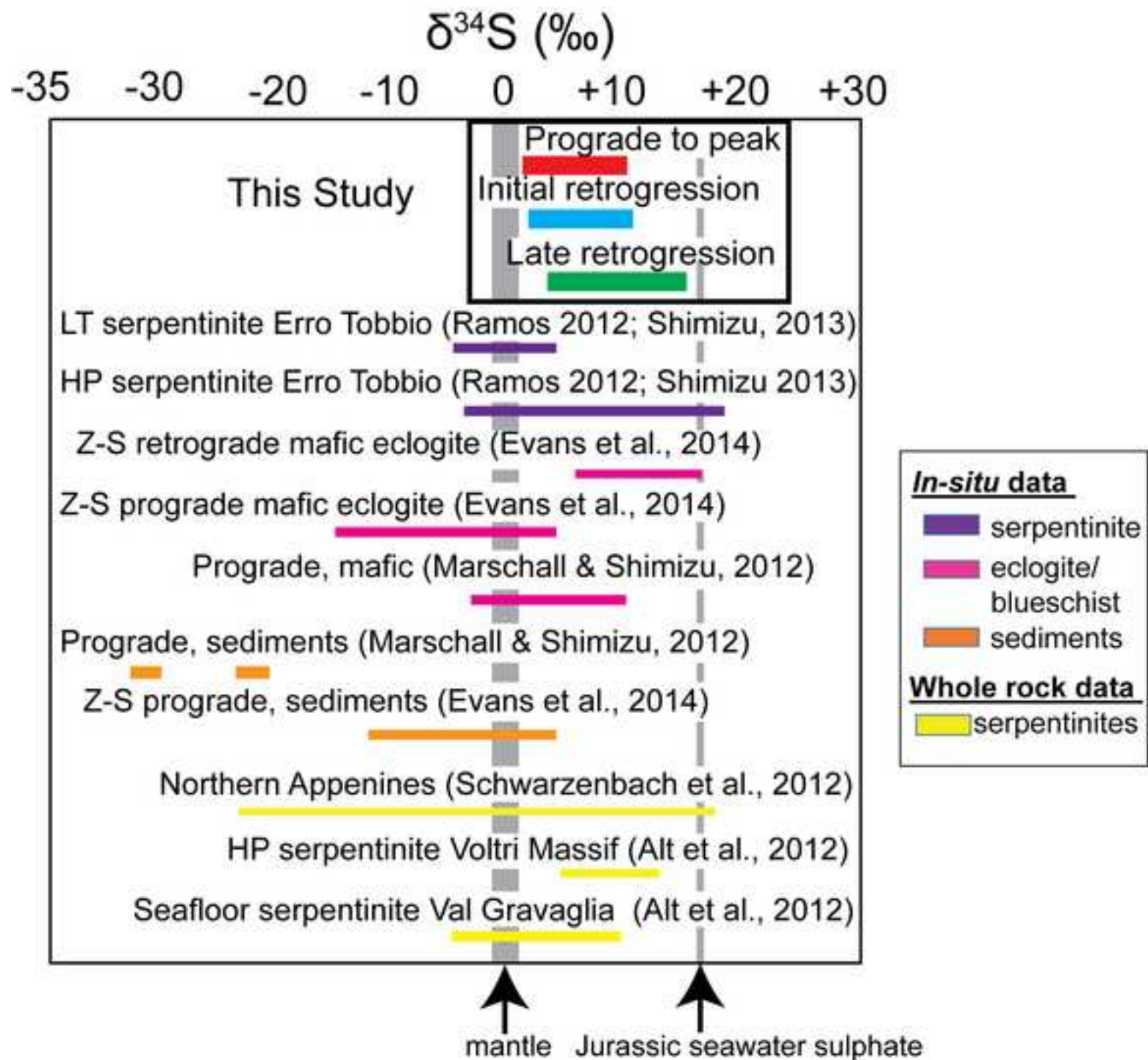**Click here to download high resolution image**

Figure 10

Figure 11

Table 1
Click here to download Table: Table 1.docx

Table 1: EPMA data for sulfides. Number in brackets is two standard deviations. b.d.l indicates the concentration is below detection

Sample	CO13-40 Pn1	CO13-33	CO13-33	CO13-33	CO13-55	CO13-55	CO13-55	CO14-03	CO14-04	CO14-04
Phase	(n=10)	Pn1 (n=6)	Pn2(n=14)	Pn3(n=10)	Pn1(n=9)	Pn2(n=8)	Pn3(n=13)	Py3(n=38)	Py1(n=21)	Py2(n=31)
wt%										
Si	n.d.	0.02(1)	0.04(3)	0.03(1)	0.05(3)	0.1(1)	0.04(4)	b.d.l	b.d.l	b.d.l
Mg	n.d.	0.09(9)	0.10(9)	0.05(4)	0.08(7)	0.07(4)	0.06(3)	b.d.l	b.d.l	b.d.l
Ni	34(2)	37.2(4)	37.1(3)	37.2(5)	37.5(8)	36(2)	37(1)	b.d.l	0.2(2)	0.2(2)
Fe	28.4(7)	25.3(4)	26.6(3)	26.1(5)	25.5(9)	26(1)	26(2)	45.3(5)	46.8(2)	46.8(4)
Co	1.8(2)	2.40(6)	2.32(5)	2.37(8)	2.3(2)	2.2(2)	2.3(2)	1.0(4)	0.1(3)	0.1(3)
S	35(2)	33.1(5)	33.3(3)	33.2(4)	33.4(2)	33.2(5)	33.3(2)	53.3(2)	53.9(3)	53.9(3)
Cu	n.d.	0.01(1)	0.1(2)	0.01(1)	0.01(1)	0.010(3)	0.01(1)	b.d.l	b.d.l	b.d.l
Se	n.d.	0.15(1)	0.01(1)	0.14(2)	0.16(1)	0.16(1)	0.15(2)	n.d.	n.d.	n.d.
Bi	n.d.	0.12(1)	0.13(1)	0.13(1)	0.13(1)	0.120(4)	0.13(1)	n.d.	n.d.	n.d.
As	n.d.	0.24(1)	0.22(2)	0.23(1)	0.27(4)	0.27(2)	0.25(3)	b.d.l	b.d.l	b.d.l
Sb	n.d.	0.02(1)	0.01(1)	0.01(1)	0.02(1)	0.02(2)	0.02(1)	0.02(1)	0.02(1)	0.01(1)
TOTAL	98.9(7)	99(1)	99.2(5)	99.7(5)	99.5(7)	98.6(7)	98.7(5)	100.4(3)	101.1(3)	101.1(3)
mol%										
Ni	26.9(8)	29.27(7)	29.1(2)	29.1(3)	29.3(6)	28(1)	29(1)	-	0.1(1)	0.1(1)
Fe	23.3(6)	21.0(2)	21.1(2)	21.4(5)	20.9(7)	22(1)	21(1)	32.5(3)	33.2(1)	33.2(3)
Co	1.3	1.88(5)	1.81(4)	1.85(6)	1.8(1)	1.7(1)	1.8(2)	0.7(3)	0.1(2)	0.1(1)
S	49(1)	47.8(2)	47.9(2)	47.5(3)	47.8(2)	47.9(3)	47.9(2)	66.79(9)	66.6(2)	66.6(2)
S/Fe+Ni+Co	0.94(5)	0.92(1)	0.92(1)	0.91(1)	0.92(1)	0.92(1)	0.92(1)	2.011(8)	2.2(2)	2.2(3)

Table 2
Click here to download Table: Table 2.docx

Table 1: Average δ^{34}S sulfur isotope analyses of individual pentlandite (pn) and pyrite (py) grains. 'Stage' corresponds to the metamorphic stage of the sulphide grain growth; P = prograde to peak metamorphism, EE = Early Exhumation, LE = Late Exhumation. The full analytical results are reported in Appendix B. N.a. = not applicable for single analyses of grains.

Grain	Sulfide	Average δ^{34}S$_{VCDT}$ (‰)	External 2σ (‰)	# Analyses	Av 2σ on single grain (‰)	Stage
CO13-40						
CO13-40-a1-s1	Pn1	7.23	1.22	3	0.98	P
CO13-40-a1-s2	Pn1	9.33	2.33	2	1.03	P
CO13-40-a1-s3	Pn1	8.80	n.a.	1	0.93	P
CO13-40-a1-s4	Pn1	4.27	n.a.	1	1.10	P
CO13-40-a2-s1	Pn1	7.57	n.a.	1	0.31	P
CO13-40-a2-s2	Pn1	5.39	n.a.	1	0.37	P
CO13-40-a2-s3	Pn1	6.32	0.35	2	0.46	P
CO13-40-a3-s1	Pn1	6.72	1.04	3	0.36	P
CO13-40-a3-s2	Pn1	5.93	0.99	2	0.46	P
CO13-40-a3-s3	Pn1	8.85	n.a.	1	0.32	P
CO13-40-a3-s4	Pn1	10.43	n.a.	1	0.90	P
CO13-40-a3-s5	Pn1	6.77	n.a.	1	1.14	P
CO13-40-a3-s6	Pn1	6.21	n.a.	1	1.09	P
CO13-40-a3-s8	Pn1	8.73	2.15	3	0.96	P
CO13-40-a3-s9	Pn1	8.81	0.04	2	0.81	P
CO13-40-a3-s10	Pn1	9.36	n.a.	1	0.86	P
CO13-40-a3-13	Pn1	8.83	n.a.	1	0.78	P
CO13-40-a3-14	Pn1	5.03	n.a.	1	0.79	P
CO13-40-a3-15	Pn1	4.39	n.a.	1	0.94	P
CO13-40-a3-16	Pn1	8.03	n.a.	1	0.82	P
CO13-33						
CO13-33-a2-s2	Pn2	5.50	n.a.	1	0.76	EE
CO13-33-a2-s3	Pn2	7.88	n.a.	1	0.74	EE
CO13-33-a2-s4	Pn2	9.19	0.81	2	0.81	EE
CO13-33-a2-s5	Pn3	3.89	n.a.	1	0.90	LE
CO13-33-a2-s6	Pn3	7.27	n.a.	1	0.75	LE
CO13-33-a2-s7	Pn3	8.42	n.a.	1	0.72	LE
CO13-33-a2-s8	Pn3	8.20	n.a.	1	0.82	LE
CO13-33-a2-s9	Pn2	7.91	n.a.	1	0.76	EE
CO13-33-a3-s1	Pn1	5.47	n.a.	1	0.78	P
CO13-33-a3-s2	Pn1	8.82	n.a.	1	0.79	P
CO13-33-a3-s4	Pn2	6.54	n.a.	1	0.73	EE
CO13-33-a3-s6	Pn2	7.54	n.a.	1	0.83	EE
CO13-33-a3-s7	Pn2	7.56	n.a.	1	0.74	EE
CO13-33-a3-s10	Pn3	1.75	n.a.	1	0.74	LE
CO13-33-a3-s13	Pn1	6.53	n.a.	1	0.74	P
CO13-33-a3-s14	Pn1	8.40	n.a.	1	0.75	P
CO13-33-a3-s15	Pn2	7.78	n.a.	1	0.76	EE
CO13-55						
CO13-55-a1-s1	Pn3	6.02	0.75	2	0.35	LE
CO13-55-a1-s2	Pn1	5.18	1.66	2	0.36	P
CO13-55-a1-s3	Pn3	5.91	n.a.	1	0.42	LE
CO13-55-a2-s1	Pn1	4.97	0.83	4	0.41	P
CO13-55-a2-s2	Pn2	3.25	0.20	2	0.38	EE
CO13-55-a2-s3	Pn2	5.90	0.82	2	0.39	EE
CO13-55-a3-s1	Pn3	7.44	0.36	2	0.36	LE
CO13-55-a3-s2	Pn1	3.13	0.22	3	0.41	P
CO13-55-a3-s2b	Pn1	2.95	n.a.	1	0.50	P
CO14-03						
CO14-03-a1-1-8	Py3	6.85	0.58	9	0.21	LE
CO14-03-a2-1-4	Py3	12.70	1.99	4	0.21	LE
CO14-03-a2-5	Py3	15.08	n.a.	1	0.21	LE
CO14-03-a2-7-8	Py3	10.30	3.93	2	0.21	LE
CO14-03-a2-9-13	Py3	8.13	1.75	5	0.21	LE
CO14-03-a3-1-2	Py3	7.79	0.29	2	0.21	LE
CO14-03-a3-3-4	Py3	11.16	3.14	2	0.21	LE
CO14-03-a3-5-6	Py3	10.54	4.20	2	0.21	LE
CO14-03-a3-7-8	Py3	7.32	0.37	2	0.21	LE
CO14-03-a3-9-11	Py3	10.17	3.26	3	0.22	LE
CO14-04						

CO14-04-a1-s1	Py2	3.96	0.20	17	0.15	EE
CO14-04-a2-s1, 1-9, 22-32	Py2	4.48	0.22	20	0.11	EE
CO14-04-a2-s2, 11-14, 21-23	Py1	4.31	0.16	7	0.11	P
CO14-04-a2-s3	Py1	5.06	0.10	1	0.10	P
CO14-04-a3-s1	Py1	5.06	0.40	3	0.10	P
CO14-04-a3-s2	Py1	5.02	n.a.	1	0.10	P

Table 3
Click here to download Table: Table 3.docx

Table 1: non zero Δ^{33}S sulfur isotope analyses in pentlandite (pn) and pyrite (py) grains.

Grain	Sulfide	$\Delta^{33}S_{VCDT}$ (‰)	2σ abs (‰)
CO13-40			
CO13-40 a3 s1-2	Pn1	0.52	0.30
CO13-40 a3 s3	Pn1	0.38	0.24
CO13-40 a3 s12-3	Pn1	0.67	0.50
CO13-55			
CO13-55 a2 s1-1	Pn1	0.33	0.23
CO13-55 a2 s3-1	Pn2	0.37	0.28
CO13-55 a3 s2-1	Pn1	0.38	0.23
CO13-55 a3 s2-4	Pn1	0.49	0.31
CO14-04			
CO14-04 s1 a1	Py1	0.11	0.10
CO14-04 s1 a2	Py2	-0.16	0.12
CO14-04 s1 a3	Py1	-0.17	0.15

Grain	Sulfide	$\Delta^{33}S_{VCDT}$ (‰)	2σ abs (‰)

Appendix A

Appendix B

Appendix C

Appendix D